CHALMERS
UNIVERSITY OF TECHNOLOGY

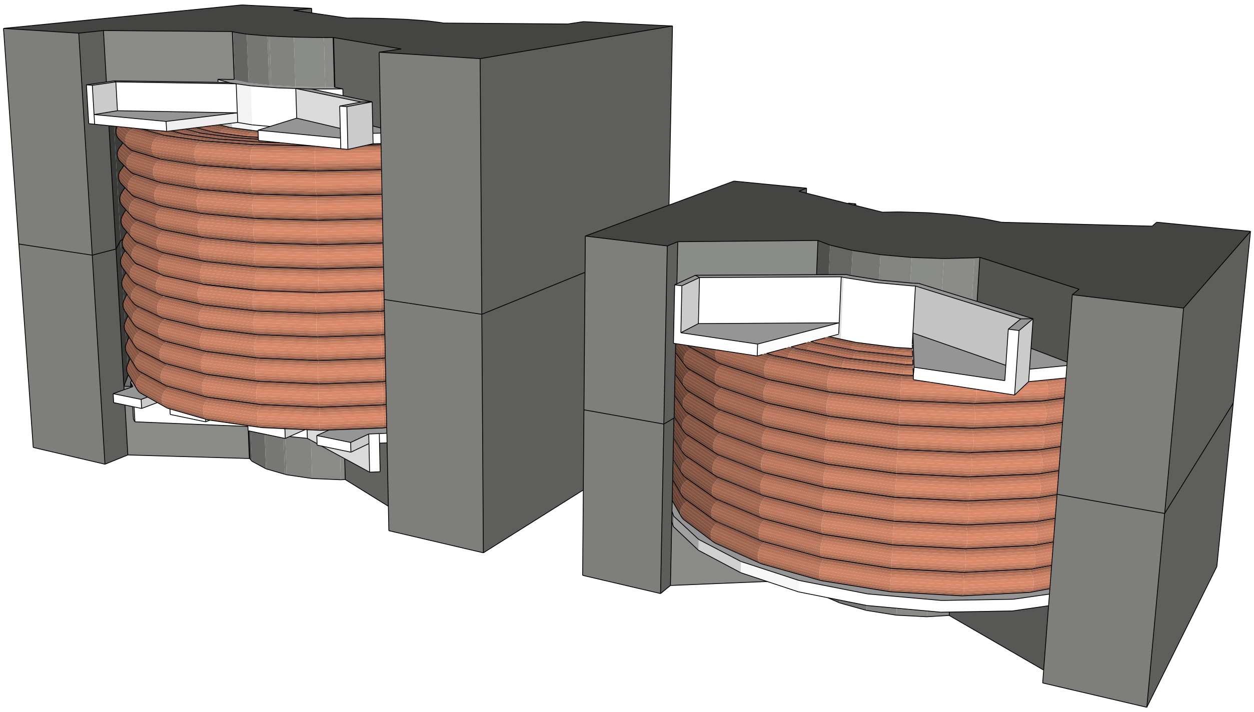

Evaluation and Design of High Frequency Transformers for On Board Charging Applications

Master's Thesis in Electrical Power Engineering

TOBIAS ELGSTRÖM
LINUS NORDGREN

Department of Energy and Environment
CHALMERS UNIVERSITY OF TECHNOLOGY

Gothenburg, Sweden 2016

Master's thesis 2016

Evaluation and Design of High Frequency Transformers for On Board Charging Applications

TOBIAS ELGSTRÖM & LINUS NORDGREN

Department of Energy and Environment
Division of Electric Power Engineering
Chalmers University of Technology
Gothenburg, Sweden 2016

Evaluation and Design of High Frequency Transformers for On Board Charging Applications
Tobias Elgström & Linus Nordgren

Supervisor: Mats Nilsson, Kongsberg Automotive
Examiner: Torbjörn Thiringer, Division of Electric Power Engineering

Master's Thesis 2016
Department of Energy and Environment
Division of Electric Power Engineering
Chalmers University of Technology
SE-412 96 Gothenburg
Telephone +46 (0)31-772 1622

Gothenburg, Sweden 2016

Evaluation and Design of High Frequency Transformers for On Board Charging Applications
TOBIAS ELGSTRÖM
LINUS NORDGREN
Department of Energy and Environment
Chalmers University of Technology

Abstract

The demand and production of hybrid and full electric vehicles is steadily increasing. This accelerates the development of infrastructure and related systems, such as chargers. When connecting the charging port directly to the grid, chargers integrated into the vehicles converts the AC mains to correct battery voltage and regulates the power. In order to achieve the required galvanic isolation of the battery from the grid, high frequency transformers are normally used. However, designing a power transformer is not trivial since its properties are highly complex to determine.

This thesis includes an investigation of the main sources of transformer winding and core losses at high frequency operation. The origin of the losses are presented in a theoretical perspective and quantified for a real case by simulations and measurements. Additionally, two identical 5.5 kW transformers for use in a 11 kW isolated DC-DC stage are designed using a loss calculation model and an optimization algorithm, both developed in this work. The transformers reach an efficiency of above 99.63 % under normal operating conditions and the losses are limited to 20.8 W in each transformer throughout the full operating range. Moreover, the power density for the designed transformer is $46\,\mathrm{kW\,dm^{-3}}$ and the total packaging volume is $0.119\,\mathrm{dm^3}$.

It is further studied how the loss characteristics depend on a multiple of parameters and operating points. Quantification of the losses clearly motivates that the harmonic content of the non-sinusoidal waveforms is non-neglectable. The reason is that, in many cases, the majority of the winding losses are caused by harmonics. It is also shown how a well constructed winding alignment and litz wire configuration significantly can reduce losses.

Keywords: Power Electronics, OBC, Charger, Transformer, Electric, Electric-Hybrid, Vehicle, Magnetics, Litz, Proximity Effect, Skin Effect, Steinmetz, Isolated DC-DC.

Acknowledgements

First of all we would like to express our gratitude to Kongsberg Automotive that has given us the opportunity to conduct this thesis and to deepen our knowledge within the field of power electronics. We would like to give a special thanks to Mats Nilsson, for his engagement and time, spent on this thesis. We would further like to express our gratitude to our examiner at Chalmers University, Professor Torbjörn Thiringer, for his time and help regarding the thesis and especially the report work. In addition we would also like to direct a special thanks to Daniel Pehrman, who have designed the converter used during the verification and supported us during the same.

Finally we would like to give a great thanks to all other people at Kongsberg Automotive and the Department of Energy an Environment at Chalmers University of Technology that has contributed with valuable insights and discussions.

Tobias Elgström & Linus Nordgren, Gothenburg, June 2016

List of Abbreviations

FEM	Finite Element Method
FFT	Fast Fourier Transform
GSE	General Steinmetz Equation
HF	High Frequency
LMS	Least Mean Square
OBC	On Board Charger
OSE	Original Steinmetz Equation
RMS	Root Mean Square
ZVS	Zero Voltage Switching

Contents

Abstract **v**

Acknowledgments **vii**

List of Abbreviations **ix**

1 Introduction **1**
1.1 Problem Background 1
1.2 Previous Work 2
1.3 Thesis Aim and Contribution 2
1.4 Limitations 2

2 Phase-Shifted Full-Bridge Isolated DC-DC Converter **5**
2.1 Topology Overview 5
2.2 Phase-Shifted Operation and ZVS 5

3 Transformer Core Losses and Characteristics **9**
3.1 Power Losses in Magnetic Materials 9
3.2 Empirical Steinmetz Equations 13
3.3 Extracting Steinmetz Parameters 13
3.4 FEM Verification of the Calculated Losses 14

4 Transformer Winding Losses **17**
4.1 DC Resistance 17
4.2 Skin Effect 17
4.3 Proximity Effect 18
4.4 Winding Configuration and Power Loss 20
4.4.1 Round Wire 21
4.4.2 Litz Wire 22
4.5 HF Resistance Dependency of Frequency 23
4.6 Optimal Number of Strands 24

5 Base Case Verification and Model Evaluation **27**
5.1 Loss Calculation Procedure 27
5.2 Base Verification 29
5.2.1 Winding Loss Measurements Setup 29
5.2.2 Measurement Results 30

5.3 Winding Loss Evaluation . . . 36
5.3.1 Impact of Waveform and Harmonics . . . 36
5.3.2 Interleaving . . . 38
5.3.3 Increased Magnetization Current due to Gap Distance . . . 38
5.3.4 Leakage Inductance and its Influence on HF Losses . . . 39
5.3.5 Impact of Strand Diameter . . . 40
5.4 Core Loss Evaluation . . . 43
5.4.1 Inhomogeneous Flux Distribution . . . 43
5.4.2 Comparison of FEM Results and Steinmetz Equations . . . 44

6 Transformer Design Proposal for an Isolated 11 kW DC-DC Stage 45
6.1 Multi-Object Optimization . . . 46
6.1.1 Design Algorithm . . . 46
6.1.2 Pareto Optimization . . . 48
6.2 Core and Winding Selection . . . 49
6.3 Loss Evaluation for Selected Core . . . 51

7 Conclusions 53
7.1 Results from Present Work . . . 53
7.2 Future Work . . . 53

Bibliography 55

1 Introduction

1.1 Problem Background

Magnetic components such as inductors and transformers have been key components in electrical systems since the first transformer was invented in the late 19th century [1]. In grid applications, where it acts as step up or step down transformer, the main requirements for the transformer are efficiency and reliability. In other applications, like audio amplifiers and power electronics, the transformer impedance and controllability are two additional design factors which have to be taken into consideration [2].

The design procedure has normally been straight forward using guides and approximations since the requirements on power density and cost have not been crucial. However, the increased demand of high power density and high efficiency transformers directed to the consumer market, solar converters, electric and hybrid vehicles have put higher requirements on the transformer and consequentially the design procedure [2].

In On Board Chargers (OBC), used within the automotive industry for charging of vehicle batteries, the transformer plays a highly important role for power transfer control and grid isolation. Compared to grid transformers, both weight and size are crucial design parameters when designing a compact transformer used in OBCs because the limited space and the impact of weight on the vehicle efficiency [2]. Usually, the most common way to reduce the size and weight of a magnetic component is to increase the frequency. However, with increased frequency additional losses will emerge in the windings, which highlights the complexity of designing transformers.

There are normally no ”off-the-rack” solutions for transformers as with resistors and capacitors and the design is always a trade-off between efficiency, size, functionality and thermal properties. The fact that many of the transformer characteristics also are interconnected, like the thermal influence on winding resistance and core permeability, complicates the design process even further. Therefore, a lot of work has been put into developing usable methods for estimating transformer losses.

1.2 Previous Work

Calculation and measurements of core losses have been made in several ways over the years. The most common analytical formulas for core loss calculations are the Steinmetz equations, developed in different stages for improving the accuracy [3, 4, 5].

Switched converters connected to the transformer will generate non-sinusoidal waveforms. These waveforms, and especially their infinite number of harmonics have to be taken into account when calculating winding losses since they are frequency dependent [6]. Resistive losses and skin effect losses are usually easily estimated whilst proximity loss calculations fast grow very complex. However, by simplifications and approximations it is possible to calculate proximity losses with high accuracy depending on winding and wire configurations [6, 7]. By means of this, it should be possible to combine this research into design algorithms based on requirements, loss calculations and optimization methods.

1.3 Thesis Aim and Contribution

The aim of this thesis is to develop an adaptive transformer model based on analytical formulas from previous research. To achieve this, the transformer winding and core losses are calculated and verified by measurements. Finally, the transformer model is used for the design of an 11 kW transformer solution for use in an isolated DC-DC stage. In short, this thesis will contribute with:

- Review of the isolated DC-DC converter fundamentals such as switching states and waveform appearance.
- Propose and verify a procedure for calculating transformer losses under different operating points.
- Quantification and presentation of transformer losses depending on current harmonic content, winding layout, core selection and power rating.
- Propose an algorithm for design and optimization of a transformer based on required specifications.
- Presentation of a transformer solution for an 11 kW isolated DC-DC stage and expected losses within a typical operating range.

1.4 Limitations

This thesis will not address the topic of thermal modeling of the transformer model. Instead the focus will be on quantifying and reducing the losses which consequently reduce the heat dissipation. This is primarily due to the fundamental difference in cooling of OBC applications from traditional cooling where forced convection is used and the lack of standardized cooling concepts for OBCs. Introducing a thermal model of the system would significantly increase the complexity of the model. It would furthermore only be valid in the particular case evaluated and not be of a more general nature, which is the aim of the design procedure presented in this thesis.

Additionally, different winding configurations influence on the leakage inductance of the transformer will not be investigated. Moreover, the thesis will not investigate what affect different semiconductors have on the performance of the transformer and the entire isolated DC-DC converter.

2

Phase-Shifted Full-Bridge Isolated DC-DC Converter

2.1 Topology Overview

In Figure 2.1 a full-bridge isolated DC-DC converter with phase-shifted operation is presented. The topology facilitates the galvanic isolation required for OBC applications at the same time as it offers a high output controllability [8].

The primary side of the converter consists of four MOSFETs that generates the High Frequency (HF) current needed for the power transfer over the transformer. On the secondary side the current is rectified via a full-bridge diode rectifier and finally supplied to the battery. By adjusting the active state, or duty cycle D as it is usually called of the converter, the output voltage can be adjusted to the entire range of the battery, which typically range between 250 V to 450 V [8, 9].

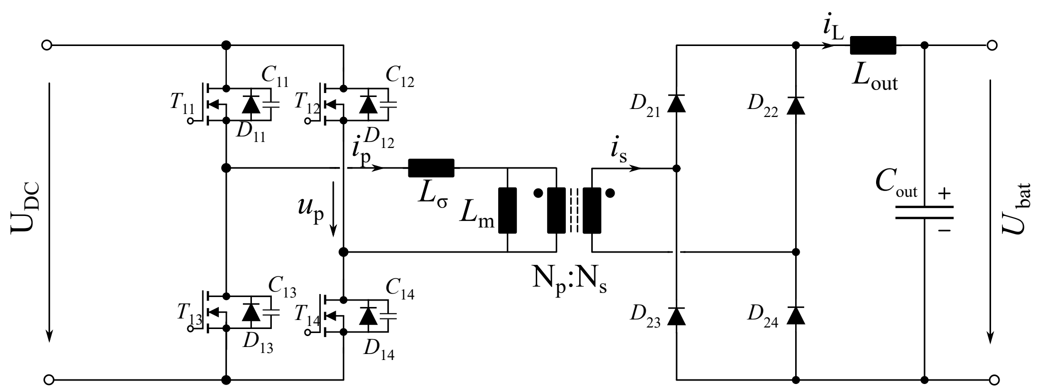

Figure 2.1: Topology of considered full-bridge isolated DC-DC converter.

In Figure 2.1, L_m and L_σ together with the ideal transformer are the electrical representation of a real transformer. L_m is the magnetizing inductance and L_σ is the leakage inductance. Furthermore, L_{out} is a output inductor that ensures a low current ripple of the output current.

2.2 Phase-Shifted Operation and ZVS

In phase-shifted operation the two bridge legs of the converter is operated with a duty cycle of 50 % ($D = 0.5$) including a small dead-band to avoid short circuiting.

The power transfer is controlled by phase-shifting one leg with respect to the other. In the following section the basic operation of the phase-shifted full-bridge converter is presented for one half cycle and the conditions under which Zero Voltage Switching (ZVS) is achieved.

Interval $t_0 < t < t_1$

In the first interval, the switches T_{11} and T_{14} in Figure 2.1 are active. During this interval voltage is applied to the circuit. The currents $i_p(t)$ and $i_s(t)$ in the circuit increases as can be seen in Figure 2.2. This is due to the positive voltage $u_p(t)$ applied over the transformer and thus also over the output inductor. The stepper increase at the primary side is due to the magnetization of the transformer. At time $t_1 = DT_s/2$ the switch T_{14} is turned off and the next interval starts.

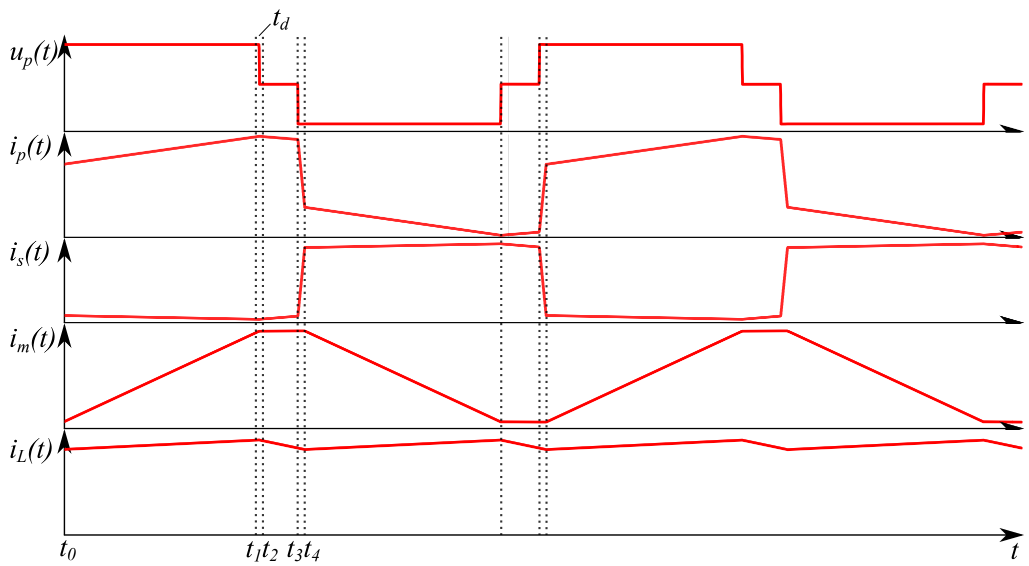

Figure 2.2: The waveforms of the full-bridge convert in phase-shift operation with ZVS.

Interval $t_1 < t < t_2$

When T_{14} is turned off the current i_p is impressed by the stray inductance L_σ and the output inductance L_{out}. The current charge C_{14} and discharge C_{12} accordingly, since they can be considered in parallel and the voltage is given by

$$U_{DC} = u_{C12} + u_{C14} = const. \longrightarrow \frac{du_{C14}}{dt} = -\frac{du_{C12}}{dt} \tag{2.1}$$

Due to the large inductance L_{out} the current $i_p(t)$ can be considered constant during the transition and the voltage increase over T_{14} is approximately linear. When C_{12} is fully discharged the parallel diode D_{12} will start to conduct and the current freewheels via T_{11} and D_{12}.

Interval $t_2 < t < t_3$

T_{12} is turned on after a small dead-band t_d at $t_2 = t_1 + t_d$ at zero voltage (ZVS). The primary winding is then considered a short circuit during the interval $t_2 < t < t_3$, where no power is transferred.

Interval $t_3 < t < t_4$

At t_3, T_{11} is turned off and a similar transition as in **Interval** $t_1 < t < t_2$ starts. The two parallel capacitors C_{11} and C_{13} will act as snubbers and ensure ZVS of T_{11}. In contrast to **Interval** $t_1 < t < t_2$, when $u_p(t)$ reach a small negative value all diodes in the output rectifier will start to conduct and the output current will freewheel through the output diodes. This will clamp the transformer voltage to a negative value corresponding to the voltage drop over the diodes. The current is then only impressed by L_σ and the assumption that $i_p(t)$ is constant is not valid in this case. To still be able to achieve ZVS, enough magnetic energy has to be stored in L_σ at t_3. The required energy for ZVS is given by [10]

$$\frac{1}{2} L_\sigma i_{p,t3}^2 \geq \frac{1}{2}(C_{11} + C_{13}) U_{DC}^2 \tag{2.2}$$

If the stored magnetic energy in L_σ is too low, the voltage u_{T13} will not decrease to zero and switching losses will occur. To ensure ZVS and proper operation of the isolated DC-DC converter it is thus important that L_σ is large enough. At low power levels ZVS of T_{13} is often lost due to the decrease of $i_p(t)$, hence the stored energy in L_σ.

3

Transformer Core Losses and Characteristics

Magnetic components, such as inductors and transformers used in electric circuits are usually the most space consuming components [2]. In automotive and aerospace applications, where compact designs together with high efficiency are crucial, it is essential with an optimal transformer design [11]. However, the reduced size of the transformer will potentially increase the losses and heat dissipation. It is therefore of great importance to be able to quantify the core losses. The use of HF inverters, as the one presented in Figure 2.1, enables decreased transformer volumes but also introduce voltage harmonics.

In this chapter the origin of the core losses and proper methods for accurate loss estimations are presented for a transformer core excited with non-sinusoidal HF voltages.

3.1 Power Losses in Magnetic Materials

Within automotive, ferromagnetic materials are commonly used because of their wide temperature range and suitability for HF applications [12]. Transformer cores are in turn available in many different geometries and designs, all of which have different properties and areas of application. When comparing different cores, properties as thermal dissipation, flux distribution, electromagnetic compatibility and available winding window will vary. Additionally, the leakage inductance, which plays an important role in the proper operation of the isolated DC-DC converter, is highly dependent on core geometry [13].

Core losses mainly consist of *hysteresis losses* due to the energy required for changing magnetization of the material and *eddy currents* due to induced currents in the material according to Faraday's law of induction. Moreover, *relaxation effect*, occurring during residual magnetization, is an additional loss component. This effect will not be investigated due to that it is mainly contributing at short duty cycles [3].

For explaining the *hysteresis losses*, a ferrite core is presented in Figure 3.1, showing the core cross section area $A_c(l_m)$ and the flux path l_m. As an example, the manufacturer provides data of permeability as a function of temperature and magnetic field density B and power loss per volume depending on magnetization, temperature and frequency.

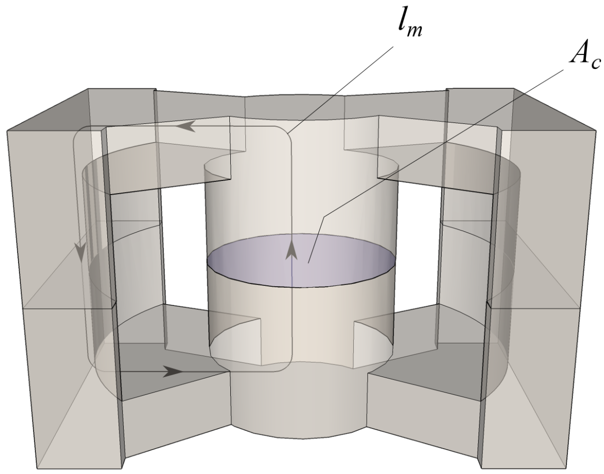

Figure 3.1: Ferrite core and the cross section area $A_c(l_m)$. The magnetic flux Φ is flowing through the center leg and splits up equally through the outer legs according to l_m.

Generally, the core losses increases with increased magnetization. This can be done by either applying lower frequency or higher magnetization voltage according to [14]

$$B = \frac{\phi}{nA_c(l_m)} = \frac{1}{nA_c(l_m)} \int_T u(t)\mathrm{d}t \tag{3.1}$$

where $A_c(l_m)$ is the cross section area of the flux path shown in Figure 3.1, ϕ is the flux linkage and $u(t)$ is the applied primary voltage. In this case, the core cross section $A_c(l_m)$ is assumed to be uniform along l_m and that B is uniform within the core.

As previously stated, changing the magnetization of the core material requires energy. Ideally all this energy is recovered in electrical form but in fact a small portion of the required energy is lost and converted into heat [14]. This energy can be represented by the hysteresis of the B-H curve, shown in Figure 3.2.

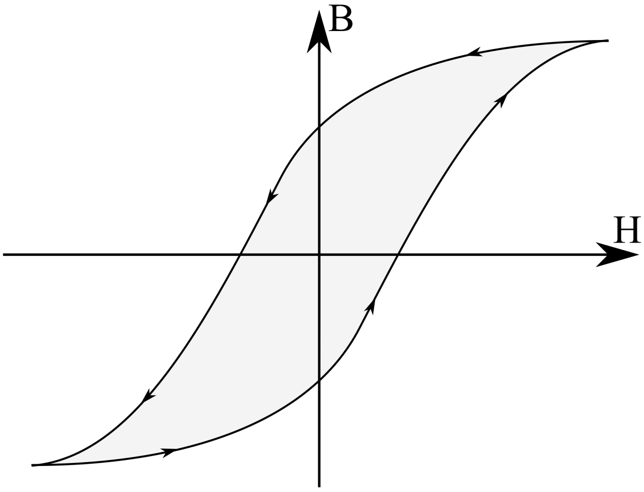

Figure 3.2: Typical hysteresis loop of the magnetic flux density B as a function of applied magnetic field H.

The total energy loss per excitation cycle can be calculated as the product of the core volume ($A_c(l_m)l_m$) and area of the B-H loop, marked in grey in Figure 3.2. For an n-turn inductor with frequency f, the energy W lost per cycle is calculated as [14]

$$W = \int_T \underbrace{\left(nA_c(l_m)\frac{dB(t)}{dt}\right)}_{\text{u(t)}} \underbrace{\left(\frac{H(t)l_m}{n}\right)}_{\text{i(t)}} \mathrm{d}t = A_c(l_m)l_m \int_T H\mathrm{d}B \tag{3.2}$$

To represent the losses as an active power loss P_c the energy W is multiplied with the excitation frequency f as

$$P_c = fA_c(l_m)l_m \int_T H\mathrm{d}B \tag{3.3}$$

Assuming that the hysteresis loop is independent of the frequency it can be concluded that the hysteresis loss is proportional to the frequency f. On the other hand, higher operating frequencies enables smaller core volumes which is desirable in many applications.

Another important loss component is the induced *eddy currents* in the material due to the alternating magnetic field. Usually, core materials are magnetic as well as electrical conductors and the magnetic field will therefore cause circulating surface currents, pursuant to the induction law, within the material. This is visualized in Figure 3.3. Accordingly, the induced eddy currents results in resistive power losses proportional to I^2R.

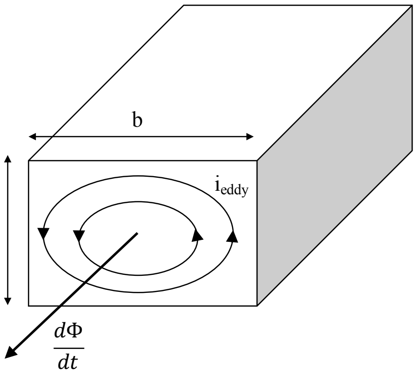

Figure 3.3: Alternating flux direction induces eddy currents within the material, hence resulting in losses.

Generally, performing loss separation calculations are difficult and instead the different types of losses are merged as total losses. Charts of the losses are usually given in datasheets provided by the manufacturer, showing total core losses depending on magnetic flux density B and frequency f. The data is extracted through tests of the magnetic material at different operating points. One example of this data can be seen in Figure 3.4 where the core loss per volume P_v as a function of magnetic flux density B.

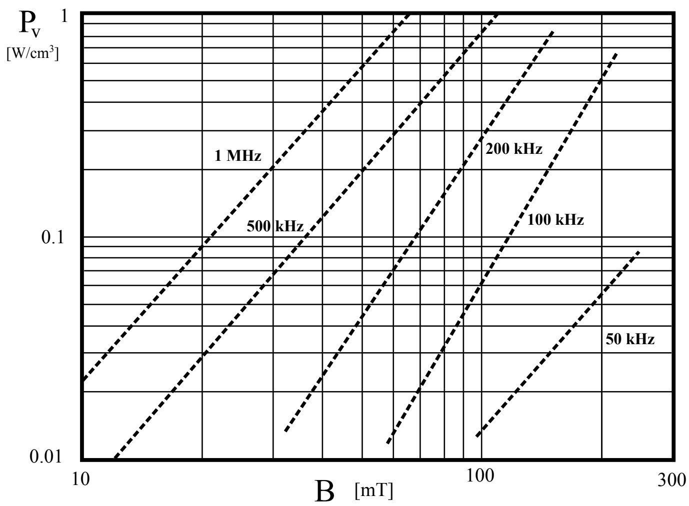

Figure 3.4: Core loss per volume at different operating points are visualized. Example of how the data is given by manufacturers.

When using datasheets for calculations of core losses, the magnetic flux density is assumed to be homogenous within the core and that the excitation voltage is a pure sinusoidal voltage.

3.2 Empirical Steinmetz Equations

In 1892, Charles Steinmetz presented an empirical equation for calculating core losses given peak flux density $\hat{B}$ [15]. The core loss per volume could, according to Steinmetz, be calculated as

$$P_v = \eta \hat{B}^{1.6} \tag{3.4}$$

where η is a hysteresis coefficient. In this case, it can be seen that the core loss are just depending on $\hat{B}$ and not frequency. The frequency dependence was later introduced and this resulted in the Original Steinmetz Equation (OSE) given as

$$P_v^{OSE} = k f^{\alpha} \hat{B}^{\beta} \tag{3.5}$$

where k, α and β can be extracted from the material specifications provided by the manufacturer. Over the years, several publications with target of improving the Steinmetz equation has been presented because of the importance of accurate core loss calculations [4, 16]. The Modified Steinmetz Equation and Generalized Steinmetz Equation (GSE) are both two versions of the equation aiming for more accurate results for non-sinusoidal waveforms and the instantaneous flux density.

The MSE and GSE were yet again revised resulting in the improved Generalized Steinmetz Equation (iGSE) in which the flux loop can be separated into one major loop and a multiple number of minor loops [5]. Still, the iGSE is applicable just using standard Steinmetz parameters α and β according to

$$P_v^{iGSE} = k_i f_{sw} \hat{B}^{\beta-\alpha} \int_0^T \left| \frac{\mathrm{d}B}{\mathrm{d}t} \right|^{\alpha} \mathrm{d}t \tag{3.6}$$

where f_{sw} is switching frequency, $\hat{B}$ is the peak flux density and k_i is defined as

$$k_i = \frac{k}{(2\pi)^{\alpha-1} \displaystyle\int_0^{2\pi} 2^{\beta-\alpha} |\cos\theta|^{\alpha} \mathrm{d}\theta} \tag{3.7}$$

where k, α and β are material and operating point specific parameters (Steinmetz parameters) that can be extracted from datasheets. The term $\cos\theta$ represent one magnetization cycle. How to extract Steinmetz parameters is further explained in Section 3.3.

3.3 Extracting Steinmetz Parameters

The core loss model used for simulations in this thesis is based on the iGSE presented in Section 3.2. This method is chosen to get the most accurate loss estimation, only using data provided by manufacturer datasheets.

Depending on f and $\hat{B}$, the Steinmetz parameters can be extracted from Figure 3.5 by selecting some points adjacent to the operating point and solve the obtained equation system using (3.5).

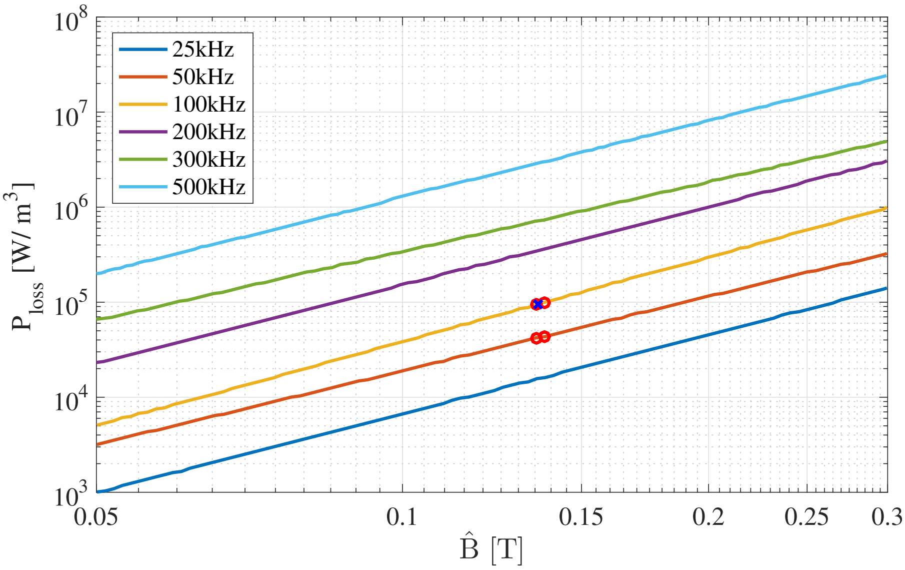

Figure 3.5: Example of Steinmetz parameters extraction for material KP95 based on peak flux and frequency. The circles represent the points for extraction and the cross shows the actual operating point.

The extracted parameters can be used in (3.6), where the peak flux density $\hat{B}$ is calculated according to (3.1) for a given operating point. The core loss per volume unit can be extracted from datasheets based on the value of $\hat{B}$ and frequency.

3.4 FEM Verification of the Calculated Losses

As previously mentioned in Section 3.1, eddy currents and hysteresis effects in the transformer core are commonly approximated using the average magnetic flux density. However, since the magnetic flux is not equally distributed in the core volume, the results obtained from analytical calculations can be compared and verified with Finite Element Method (FEM) analysis.

In FEM the core geometry can be modeled in 3D and divided into finite elements. Accordingly, the specific flux density for finite elements is linked with the data from material datasheets and the total core loss can be summarized. When performing simulations of the core geometry and its corresponding material several calculations of entities can be made. Moreover, the magnetization inductance, magnetization current and average flux density may be determined by applying integral operations or average functions.

However, modeling of core losses is difficult because the core losses also influences the current. This phenomena is particularly evident in transformers at high magnetization without air-gaps [17]. It is also important to emphasize that the FEM calculations accuracy are highly dependent on accurate data inputs such as geometries and material specifications.

4

Transformer Winding Losses

4.1 DC Resistance

When direct current flows in a conductor, the resistivity of the conductor gives rise to losses. This is referred to as the DC resistance of a conductor and is calculated by

$$R_{DC} = \frac{4l}{\sigma \pi d^2} \tag{4.1}$$

where l is the length of the conductor, d is the diameter and σ is the electric conductivity of the conductor material. The conductivity is in turn dependent on the temperature of the material and given by

$$\sigma(T) = \frac{1}{\rho(1 + \alpha_T(T - T_{ref}))} \tag{4.2}$$

where ρ is the resistivity coefficient at T_{ref} and α_T is the temperature coefficient of the material. For an increase in temperature the conductivity of the conductor is reduced.

4.2 Skin Effect

When a current $i(t)$ flows through a conductor it gives rise to a magnetic field $H(t)$ [14, 18], according to Figure 4.1. HF currents flowing in a conductor will in accordance to Lenz's law induce eddy currents that oppose the magnetic field $H(t)$. Figure 4.1 shows how the net current density in the middle of the conductor is reduced, whilst it is increased at the surface of a conductor. Therefore, at high frequencies the effective copper area of a conductor will be reduced, thus increasing the losses.

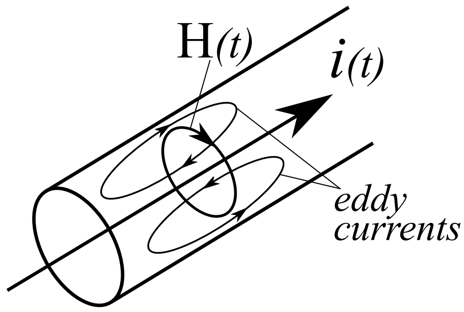

Figure 4.1: Induced eddy currents in a round conductor due to a HF current.

The current density in the center of the conductor is reduced exponentially with the distance to the surface of the conductor. The depth at which the current amplitude is reduced by a factor of $^1/_e$, where e is the natural logarithm. This is usually referred to as the *skin depth* and is defined as

$$\delta = \sqrt{\frac{1}{\sigma \pi \mu_0 \mu_r f}} \tag{4.3}$$

where μ_0 is the magnetic permeability constant, μ_r the relative permeability of the conductor material (copper and aluminium $\mu_r = 1$), and f is the frequency of a sinusoidal current.

The power loss due to skin effect (including DC loss) can be calculated with [6, 19]

$$P_S = R_{DC} F_R(f) \hat{I}^2 \tag{4.4}$$

where R_{DC} is the DC resistance, $\hat{I}$ is the amplitude of the sinusoidal current and $F_R = R_{AC}/R_{DC}$ is a factor that describes the effect of conductor resistance due to skin effect. The formula for calculating F_R is given by

$$\begin{aligned} F_R(\xi) = \frac{\xi}{4\sqrt{2}} \Big[& \frac{ber_0(\xi) bei_1(\xi) - ber_0(\xi) ber_1(\xi)}{ber_1(\xi)^2 bei_1(\xi)^2} \\ & - \frac{bei_0(\xi) ber_1(\xi) - bei_0(\xi) bei_1(\xi)}{ber_1(\xi)^2 bei_1(\xi)^2} \Big] \end{aligned} \tag{4.5}$$

where ξ is defined as

$$\xi = \frac{d}{\sqrt{2}\delta} \tag{4.6}$$

with d as the diameter of the conductor and δ the skin depth. The formula is based on a Bessel differential equations and the derivation of (4.4) and (4.5) are found in [19] for the interested reader.

4.3 Proximity Effect

In multilayer components such as transformers and inductors the copper losses exceed those introduced by skin effect alone. The magnetic field $H(t)$ produced by a HF current in a conductor is not limited to affect the conductor itself, but will also affect conductors in a close proximity. As can be seen in Figure 4.2, the magnetic field of the upper conductor penetrates the lower conductor and induce eddy currents that will increase the net current density on one side of the conductor and decrease it on the other.

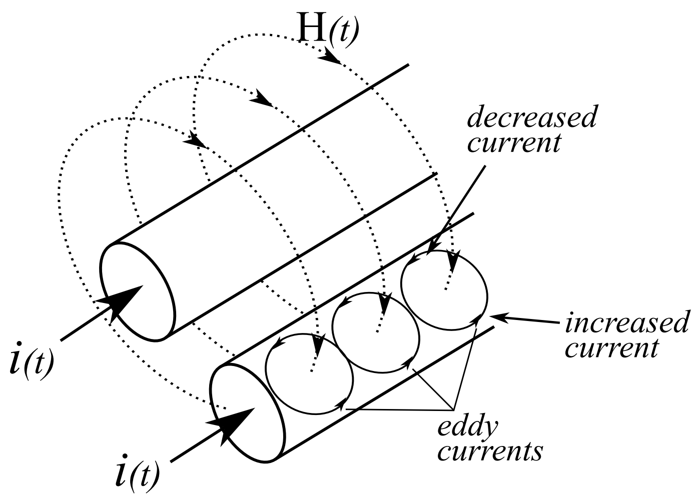

Figure 4.2: Principle of proximity effect where the magnetic flux of the upper conductor induce eddy currents in the lower conductor according to Lenz's law.

The influence two conductors carrying current have on each other is dependent on the direction of the currents and is shown in Figure 4.3. In (a) the net currents have the same direction and the current density is increased at the outside of the two conductors (red color). In (b), the currents have opposite directions and the opposite holds true where, the current density is increased at the inside of the conductors (red color). It should be pointed out that the proximity effect causes circulating currents within the conductors and that the current density is presented with its absolute value in Figure 4.3. However, the net current is set to a constant value I.

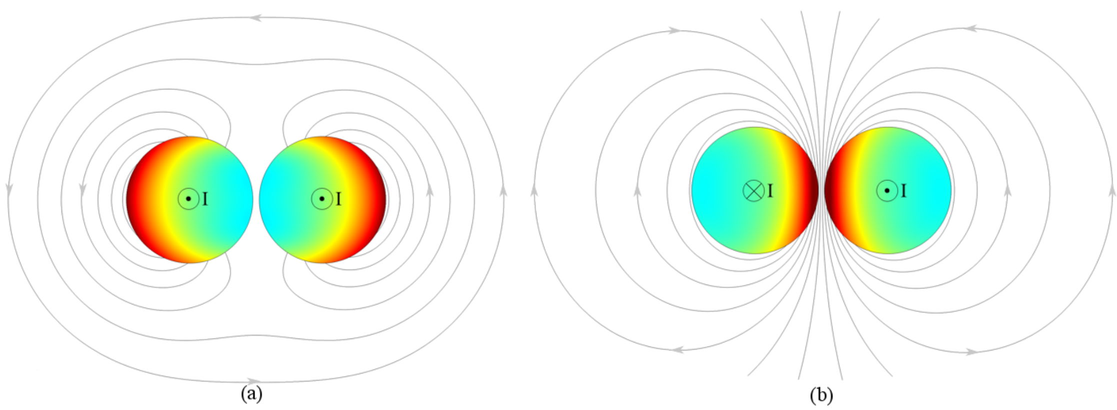

Figure 4.3: (a) Current density and magnetic field distribution for two conductors carrying current in the same direction. (b) Current density and magnetic field distribution for two conductors carrying current in the opposite direction.

The power loss in a conductor due to proximity effect is calculated as [6]

$$P_P = R_{DC} G_R(f) H_{ext}^2 \tag{4.7}$$

with

$$\begin{aligned} G_R(\xi) = -\frac{\xi \pi^2 d_{cu}^2}{2\sqrt{2}} \Bigg[& \frac{ber_2(\xi) ber_1(\xi) + ber_2(\xi) bei_1(\xi)}{ber_0(\xi)^2 bei_0(\xi)^2} \\ & - \frac{bei_2(\xi) bei_1(\xi) - bei_2(\xi) ber_1(\xi)}{ber_0(\xi)^2 bei_0(\xi)^2} \Bigg] \end{aligned} \tag{4.8}$$

The derivation of (4.7) and (4.8) are also found in [19].

4.4 Winding Configuration and Power Loss

The HF losses in a conductor are as discussed in the previous section dependent on the magnetic field penetrating the conductor. In a multilayer transformer the magnetic field distribution is highly dependent on the winding configuration, hence the overall winding losses. In Figure 4.4 two different winding configurations and corresponding magnetic field are presented. In Figure 4.4, N_L is the number of turns per layer and M_L is the number of adjacent layers with the same current direction. It should be noted that the magnetic field distribution in Figure 4.4 is only valid when $\delta \approx d_{cu}$ and the current distribution is homogeneous [18]. In (a) the primary winding is wounded on to the bobbin first and then the secondary is wounded outside the primary. The winding configuration results in a high magnetic field between the primary and secondary winding with a large current displacement as a result. In (b) the primary and secondary windings are wounded interleaved which significantly reduces the magnetic field H and hence, lowering the current displacement and the losses due to proximity effects.

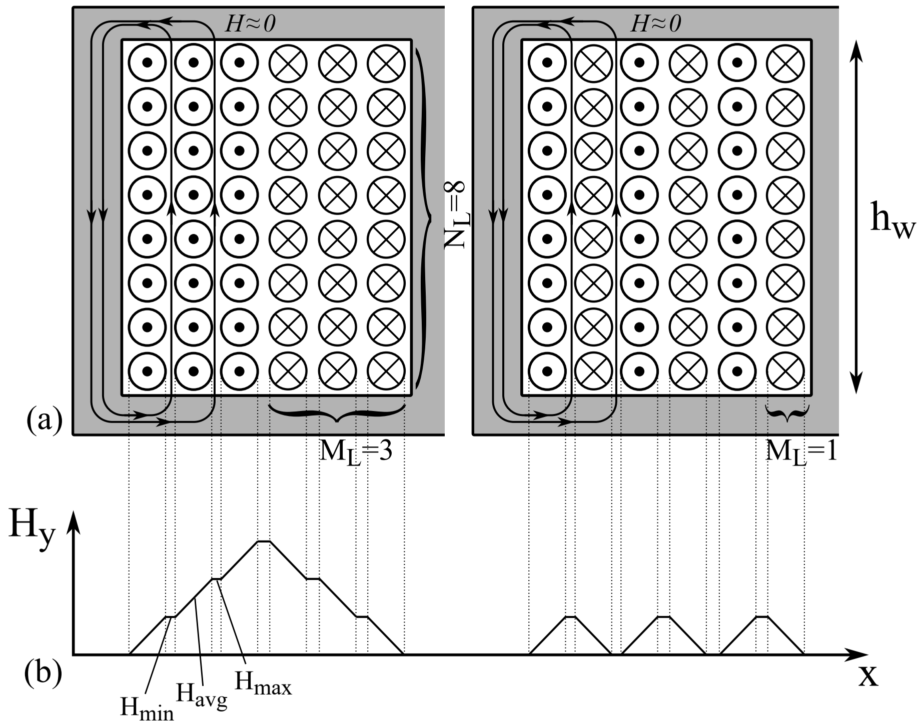

Figure 4.4: (a) Two different winding configuration (non-interleaved and interleaved). (b) Corresponding magnetic field H distribution for the two transformer windings in (a).

The average magnetic field $\hat{H}_{avg}$ in a conductor with $\delta \approx d_{cu}$ can be calculated as

$$\hat{H}_{y,avg} = \frac{1}{2}(\hat{H}_{y,min} + \hat{H}_{y,max}) \tag{4.9}$$

with a winding configuration as in Figure 4.4 the average magnetic field $\hat{H}_{avg}$ can further be calculated as

$$\hat{H}_{y,avg} = \frac{2m-1}{2}\frac{N_L\hat{I}}{h_w} \tag{4.10}$$

with $m = 1, 2, ..., M_L$ and where M_L is the number of adjacent layers with the same current direction, N_L is the number of turns per layer and h_w is the height of the core window..

4.4.1 Round Wire

Total winding losses in transformer winding

$$\begin{aligned} P_{RW} &= R_{DC}\Big(F_R\hat{I}^2 + \frac{G_R}{M_L}\sum_{m=1}^{M_L}\hat{H}_{avg}(m)^2\Big) \\ &= R_{DC}\hat{I}^2\Big(F_R + N_L^2 G_R\frac{4M_L^2-1}{12h_w^2}\Big) \end{aligned} \tag{4.11}$$

where M_L is the number of adjacent layers with the same current direction and N_L is the number of turns per layer.

4.4.2 Litz Wire

To reduce the winding losses in HF applications, litz wires can be used. Litz wires are conductors that in turn consists of thin individually-insulated strands. This significantly limits the effect of eddy currents and current displacement by using strands with a radius close to the skin depth of the current. The strands are also twisted in a way that each strands ideally occupies every position in the conductor or bundle. If correctly twisted this eliminates the bundle level skin effect that otherwise would occur [6]. The skin effect is then only present on the strand level. The skin effect losses, including DC losses for a wire of n_s strands and a strand diameter of d_{cu} can be calculated as [6, 19]

$$P_S = n_s R_{DC} F_R \left(\frac{\hat{I}}{n_s} \right)^2 \tag{4.12}$$

with R_{DC} and F_R calculated as in (4.1) and (4.4) with $d = d_{cu}$.

Litz wires are in the same way as round wires affected by the magnetic field H_{ext} from adjacent conductors, but in addition also by internal magnetic field H_{int}. This is illustrated in Figure 4.5, where both the internal and external fields act on the conductor.

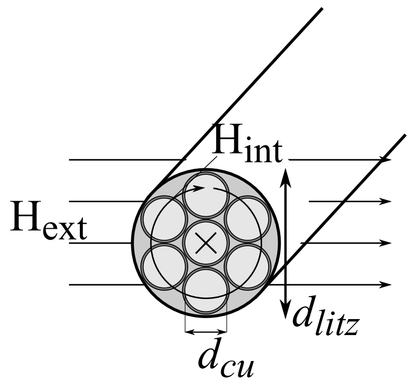

Figure 4.5: Internal and external proximity effects affecting a litz wire.

The losses due to the external magnetic field are calculated in the same way as in the case for a solid round conductor. For the calculation of the losses of the internal magnetic field it is assumed that the current is equally distributed across the cross-section of the litz wire. It is furthermore assumed that each strand is penetrated by the average internal magnetic field and that any magnetic field introduced by induced eddy currents are neglected. That is, according to [6, 20], valid if the conductor radius is less than 1.6 times the skin depth δ. Then the proximity effect losses in a litz wire is calculated as [6, 19]

$$\begin{aligned} P_P &= P_{P,ext} + P_{P,int} \\ &= n_s R_{DC} G_R \Big(\hat{H}_{ext}^2 + \frac{\hat{I}^2}{2\pi^2 d_{litz}^2} \Big) \end{aligned} \tag{4.13}$$

with R_{DC} and G_R calculated as in (4.1) and (4.7), with $d = d_{cu}$.

The total power loss in litz wire winding is finally calculated as

$$P_{LW} = R_{DC}\hat{I}^2 \Big[F_R + G_R n_s \Big(\frac{1}{\pi^2 d_{litz}^2} + \frac{N_L^2(4M_L^2 - 1)}{12h_w^2} \Big) \Big] \tag{4.14}$$

and simplified to

$$P = R_{AC}\hat{I}^2 \tag{4.15}$$

with

$$R_{AC} = R_{DC} \Big[F_R + G_R n_s \Big(\frac{1}{\pi^2 d_{litz}^2} + \frac{N_L^2(4M_L^2 - 1)}{12h_w^2} \Big) \Big] \tag{4.16}$$

where n_s is the number of strands, d_{litz} is the wire diameter, N_L is the number of turns per layer, M_L is the number of adjacent layers with the same current polarity, and h_w is the height of the core window.

4.5 HF Resistance Dependency of Frequency

Both the skin effect and the proximity effects are dependent on the frequency according to (4.5) and (4.8). The effective resistance for a litz wire of 225×0.1 mm strands, as a function of frequency, is presented in Figure 4.6. It is evident that the effective resistance is significantly increased with increasing frequency, where the largest contributions is due to the internal and external proximity effects. It should be pointed out that the proximity effects are highly dependent on the selected wire and winding configuration. So no general conclusion about which of the two effects that is dominating can be drawn.

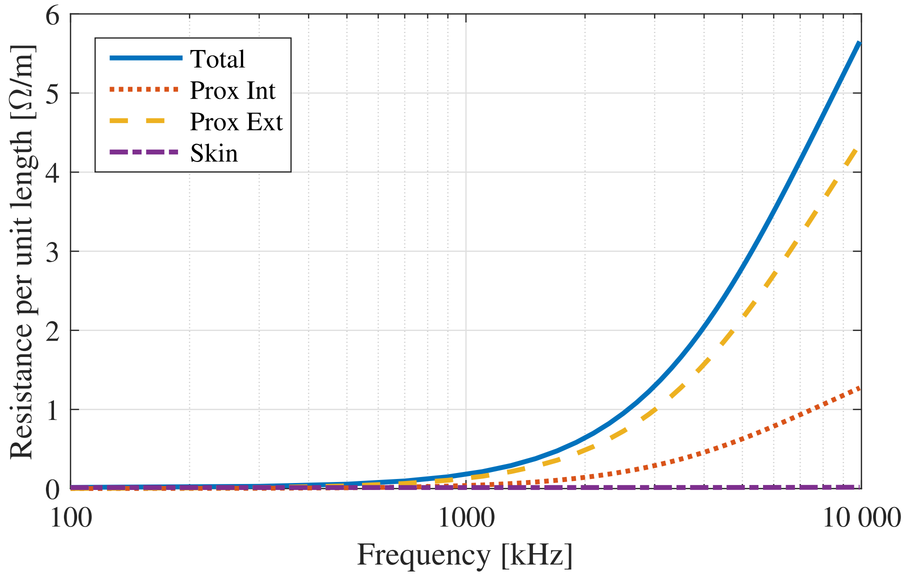

Figure 4.6: Example of the AC resistance per unit length for a transformer winding as a function of frequency. The winding configuration is the one of the test transformer described in Chapter 5.

The square waveform of the currents in switched converters introduces a infinite number of harmonics on top of the switching frequency. These harmonics have a significantly lower current amplitude than the fundamental component, but due to the increased effective resistance at HF seen in Figure 4.6, they still introduce losses that can have a significant contribution to the losses and therefore can not be neglected.

In Figure 4.7 the harmonic representation and the Fast Fourier Transform (FFT) of the first ten harmonics of a typical waveform are presented. In Figure 4.7(b) it can be seen that the harmonics only consists of the uneven harmonics, which is due to the half wave symmetry of the wave.
The power loss from an arbitrary waveform can be calculated as a sum of all its frequency harmonics as

$$P_W = R_{DC} I_{DC}^2 + \sum_{n=1}^{\infty} R_{AC}(nf_0) I_{AC}^2(nf_0) \tag{4.17}$$

where f_0 is the fundamental frequency of the waveform.

4.6 Optimal Number of Strands

The use of litz wire in HF transformers and inductors introduces another degree of freedom in the design. If a too large strand diameter is used the skin effect will reduce the effective copper, hence increase the losses. If instead a too small strand diameter is used the effective copper area will instead be limited by the increased

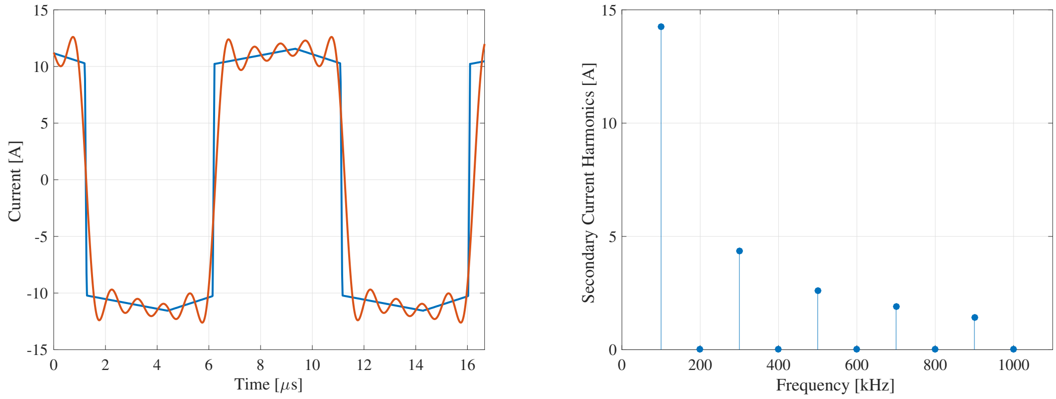

(a) (b)

Figure 4.7: (a) The secondary current waveform and the Fourier series representation considering ten harmonics. (b) The frequency spectrum of the waveform in (a).

occupation of insulation, since the insulation does not scale proportionally with the diameter [7]. For this reason an optimal number of strands can be found for a conductor of fixed outer diameter.

The correlation between strand diameter and insulation thickness can instead be approximated by [7]

$$d_t = d_r \alpha \left(\frac{d_{cu}}{d_r} \right)^{\beta} \tag{4.18}$$

where d_t is the overall strand diameter, d_{cu} is the diameter of the bare copper strand, and d_r is an arbitrary reference diameter to make α and β unitless. The parameters α and β can then be found by means of Least Mean Square (LMS) optimization on wire data from manufacturers. The number of strands can then be calculated as a function of strand diameter d_{cu} and conductor diameter d_{litz} as [7]

$$n_s = k_f \left(\frac{1}{\alpha d_r^{1-\beta}} \frac{d_{litz}}{d_{cu}^{\beta}} \right)^2 \tag{4.19}$$

where k_f is another wire specific parameter obtained by LMS.

In Figure 4.8 the AC and DC resistance for a conductor is shown as a function of strand diameter d_{cu} and f =100 kHz. It can clearly be seen that there is an optimal number of strands that minimizes the losses in the conductor, which in this case is located around 0.08 mm.

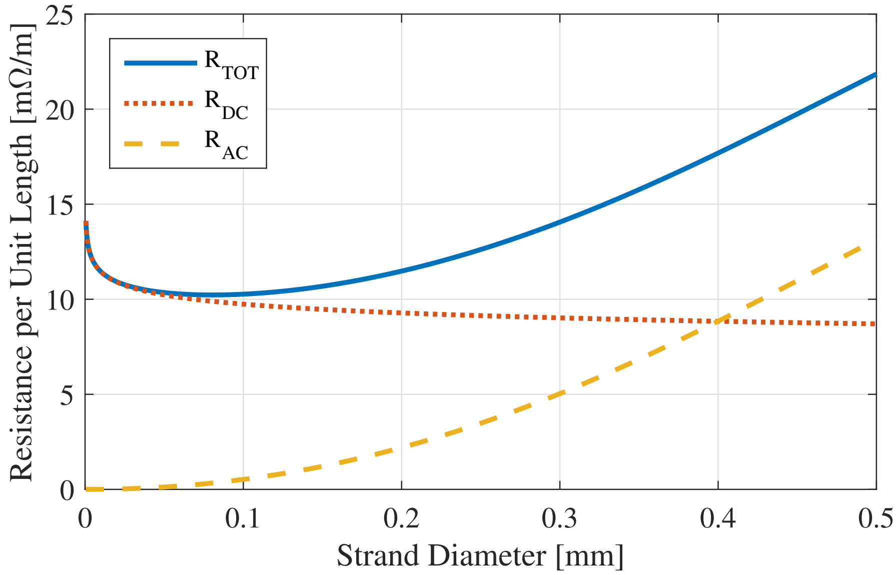

Figure 4.8: An example of the impact on AC and DC resistance for different strand diameters, for a litz wire with fixed outer diameter of 2 mm and a sinusoidal current with frequency 100 kHz.

5

Base Case Verification and Model Evaluation

The transformer model is developed in Matlab and based on the analytic formulas presented in Chapter 3 and Chapter 4. An analytic model was chosen to have a model that can easily be optimized for several different input parameters without extensive computational effort. FEM simulations were then used to further evaluate specific designs and were performed using COMSOL Multiphysics.

5.1 Loss Calculation Procedure

In Figure 5.1 the procedure for calculating losses is presented. The procedure starts with defining the electrical properties of the system and the core. This is where the system properties, such as input voltage U_{in}, output voltage U_{out}, the turns ratio n and output power P_{out}, are specified.

In the second stage the litz wire is selected and the wire length of the windings are calculated. The hitherto defined properties are used for creating the voltage and current waveforms required for loss calculations, as well as the magnetic flux density $B(t)$. Alternatively, waveforms can be imported from an external source, thus using real or simulated waveforms.

The temperature T is used for calculation of the frequency dependency of the winding losses according to the equations found in Chapter 4. By performing FFT on the currents $i_p(t)$ and $i_s(t)$, the winding losses are calculated according to (4.17) in stage 4. The number of harmonics taken into consideration can be modified from zero to infinity and are in this case set to 200.

Finally, in stage 5 and 6 the Steinmetz parameters are extracted based on operating point and then used for calculation of the core losses according to (3.6). When all properties are calculated the results are presented.

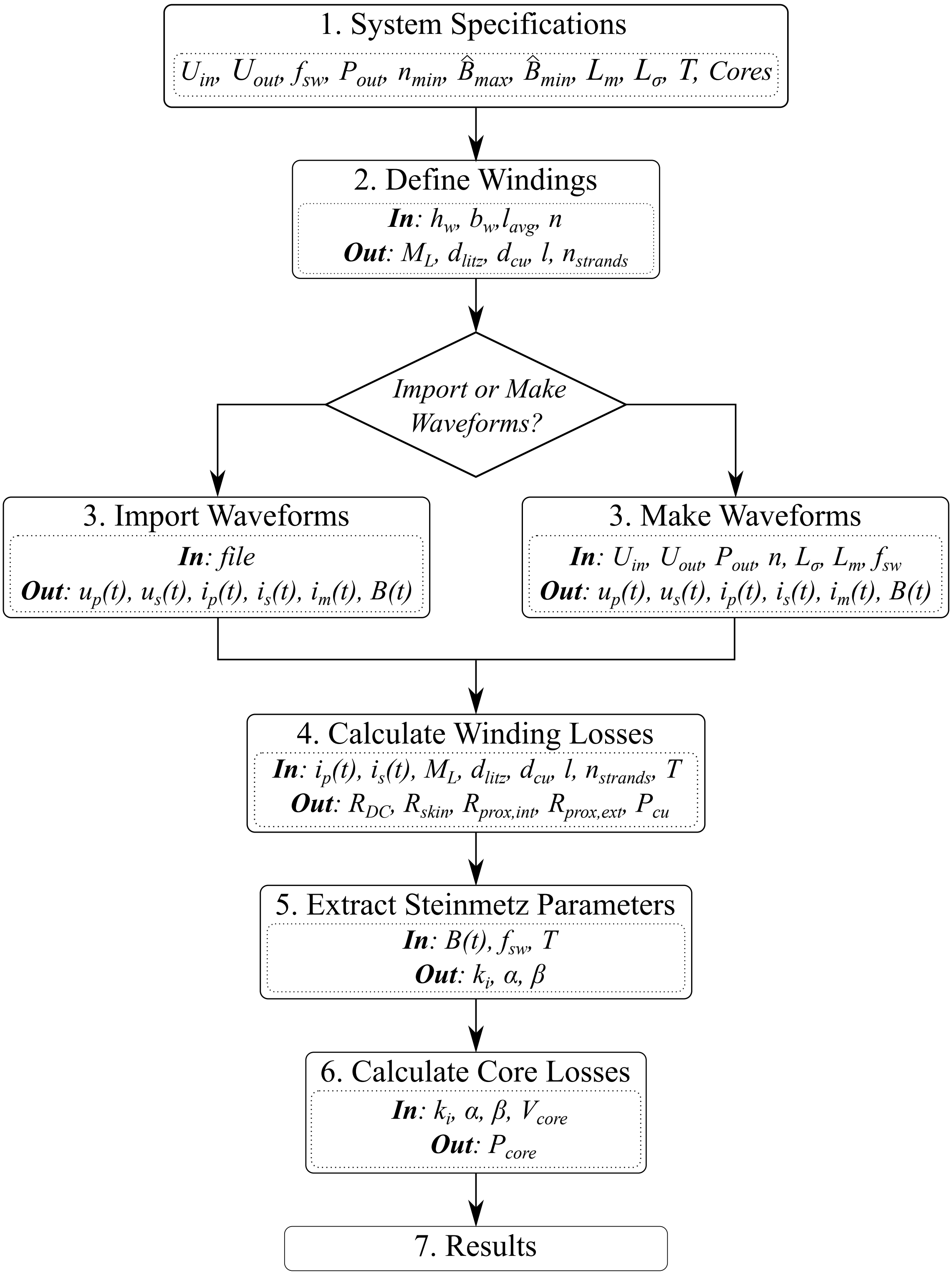

Figure 5.1: Flow chart presenting the procedure for calculating both winding and core losses depending on input specifications. In each step the ingoing parameters or conditions are displayed together with the output parameters.

5.2 Base Verification

Before using of the developed model in transformer design, the model was evaluated on an existing transformer. The evaluation was performed by simulations and lab measurements. The transformer used for evaluation has a power rating of 3.5 kW with a PQ 50/35 core of ferrite material KP95 and winding of 225 × 0.1 mm litz wire with a turns ratio of 14/16.

5.2.1 Winding Loss Measurements Setup

The measurements of the winding losses were performed using thermal measurements. This method was chosen, rather than measurements of the losses based on the electrical properties, due to the difficulty of measuring instantaneous power in HF applications. This is because of the delays introduced in transducers, primarily in the current probes.

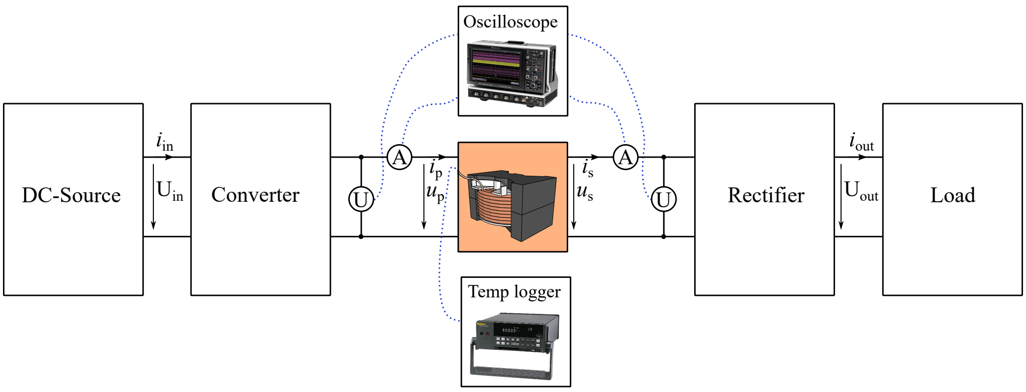

Figure 5.2: Schematic overview of the winding losses measurement setup.

Measurements were performed using a two step procedure. First an AC current was applied to the transformer, which was maintained until a steady-state temperature was reached, which for the different test ranged from 35 °C to 75 °C. The current and voltage waveforms were captured for use in the model, i.e. for calculating the winding losses.

In the second step the two windings of the transformer were short circuited and a DC current was applied to the circuit. The current was adjusted so that the same steady-state temperature as in step one was reached. The voltage and current in the transformer was then used to calculate the power loss. In this way the losses were estimated without the need of thermal modeling or high precision transducers for measurement of the electric properties.

During the tests the transformer was air cooled with a fan and the temperature was registered with a PT100 sensor embedded in the windings.

The DC source voltage was limited to 200 V during the AC test. This was primarily done to minimize the impact of core losses on the measurements. With the chosen excitation, the core losses were limited to under 1 W for all measurements. The low voltage also ensures that the voltage stress on the output diode rectifier was limited, which otherwise would exceed the rating of the diodes due to the lack of snubber circuits in the test setup.

5.2.2 Measurement Results

An example of the waveforms obtained during the tests is seen in Figure 5.3. When comparing with the ideal waveforms shown in Figure 2.2 some differences can be observed. There are mainly three properties of the measured waveforms that are not present in the ideal waveforms. Firstly, the primary voltage peak before the transition to an active state is due to a large dead-band during the transition between the upper and lower transistor. Therefore the parasitic capacitances of the transistors are both energized and drained before the transistor is turned on and ZVS is lost.

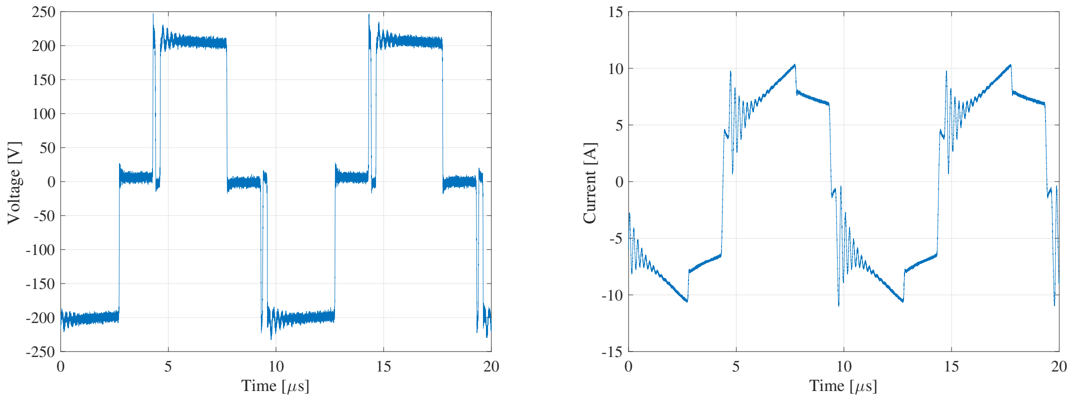

(a) (b)

Figure 5.3: (a) Primary voltage waveform. (b) Primary current waveform. The waveforms corresponds to the measurements performed in Test 1.3, where the input voltage is 200 V, the duty cycle 0.7 and the output current 6.67 A.

Secondly, in Figure 5.4(b), HF oscillations in the order of 5 MHz can be observed. Those are not present in the ideal case. The reason for this is because of parasitic capacitances in the rectifier diodes that creates a resonance circuit with the leakage inductance on the secondary side of the transformer. To decrease these oscillations, thus reducing HF losses, snubbers can effectively be utilized. Lastly, the parasitic capacitances also causes a rapid current drop in the transition from active to free wheeling state, first time seen at 2.6 µs. Increasing the excitation voltage also increases the voltage oscillations and accordingly the HF current harmonics. Because of this, depending on the amplitude of the harmonics, the optimal strand diameter giving the lowest losses may vary.

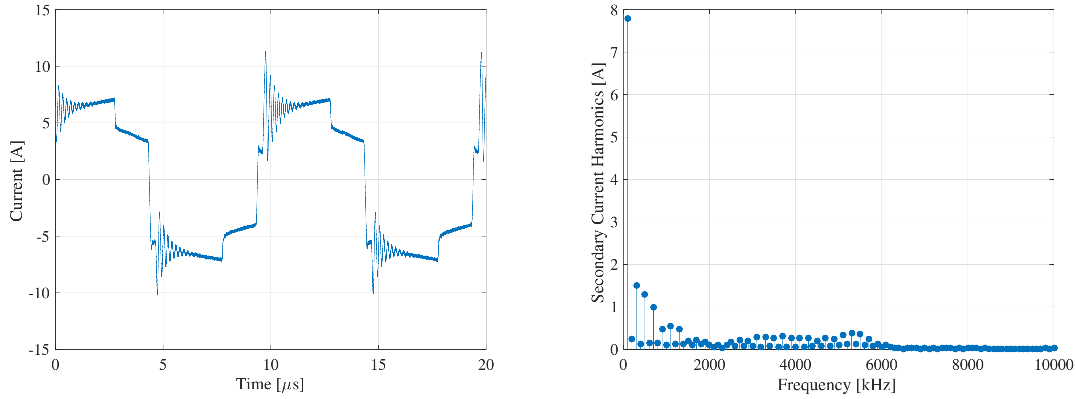

(a) (b)

Figure 5.4: (a) Secondary current current waveform during Test 1.3. (b) Harmonic distribution of the current waveform in (a).

Test 1 - Variation of Duty Cycle

In Test 1, presented in Figure 5.5 and Table 5.1, the dependency of duty cycle is evaluated. During the test, the switching frequency was set to 100 kHz, the input voltage to 200 V and the output resistance to 20 Ω. It can be seen that the calculated and measured losses correlate with high accuracy.

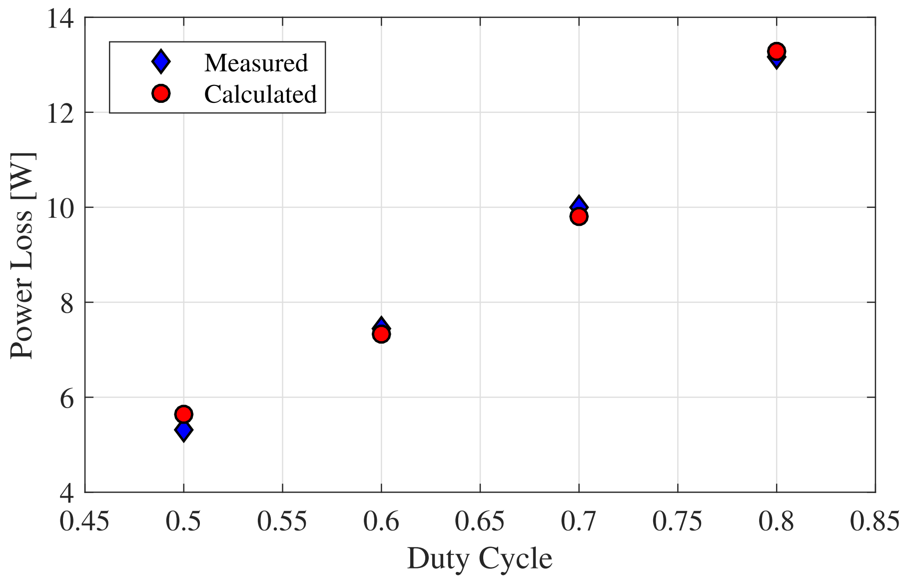

Figure 5.5: Evaluation of model for constant input voltage of 200 V, frequency of 100 kHz and output resistance of 20 Ω.

By increasing the duty cycle the windings are conducting higher currents and losses are therefore increasing. It should be noted that the active power transfer is also increased with increasing duty cycle.

Table 5.1: Losses with varying duty cycle and constant input voltage 200 V, frequency of 100 kHz and output resistance 20 Ω.

Test #	Duty Cycle	Output Cur	Meas. Loss	Calc. Loss	Error
1.1	0.5	4.4 A	5.3 W	5.6 W	5.7 %
1.2	0.6	5.6 A	7.4 W	7.3 W	1.4 %
1.3	0.7	6.7 A	10.0 W	9.8 W	2.0 %
1.4	0.8	7.8 A	13.2 W	13.3 W	0.8 %

Test 2 - Variation of Switching Frequency

Test 2 was performed by varying the frequency instead of the duty cycle, which in this case was fixed to $D = 0.7$. Input voltage and output resistance were kept at the same values as previously. Also in this case the error between the measured and calculated losses are small as can be seen in Figure 5.6 and Table 5.2.

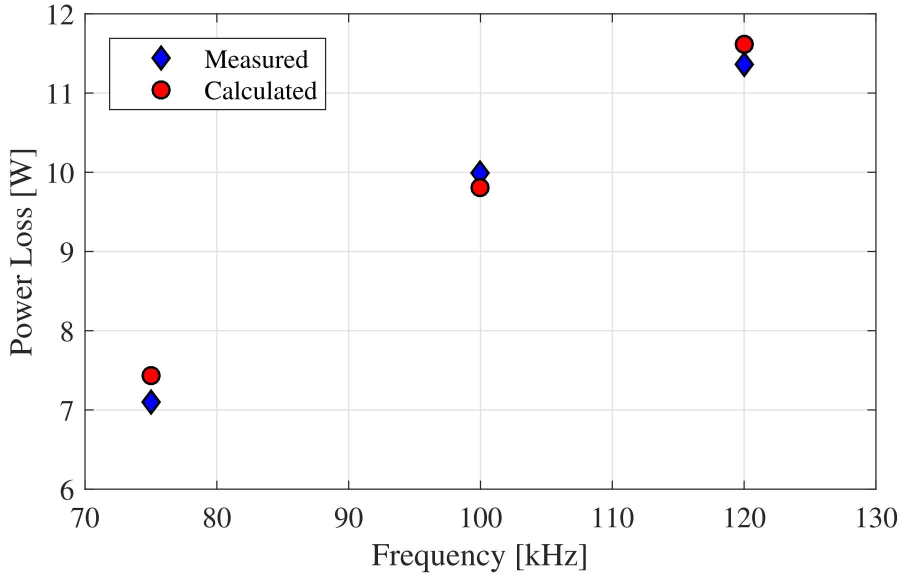

Figure 5.6: Evaluation of model with constant input voltage of 200 V, duty cycle of 0.7 and output resistance of 20 Ω.

The increased frequency results in higher magnitude of the winding losses, mainly caused by the proximity effect, according to the increased HF resistance shown in Figure 4.6. The skin effect resistance will also increase, although not at the same rate as the proximity resistance.

Table 5.2: Losses with varying frequency and constant input voltage 200 V, duty cycle 0.7 and output resistance 20 Ω.

Test #	Freq.	Output Cur	Meas. Loss	Calc. Loss	Error
2.1	75 kHz	7.1 A	7.1 W	7.5 W	5.6 %
2.2	100 kHz	6.7 A	10.0 W	9.8 W	2.0 %
2.3	120 kHz	6.5 A	11.4 W	11.6 W	1.8 %

Test 3 - Variation of Input Voltage with $I_{out} = 6.67$ A

The last two tests (Test 3 and Test 4) were performed by changing the input voltage of the converter. The load was set to constant current instead of constant resistance. In Test 3 the output current was set to 6.67 A. In Figure 5.7 it can be seen that the measured and calculated losses at 150 V deviates more than the other points.

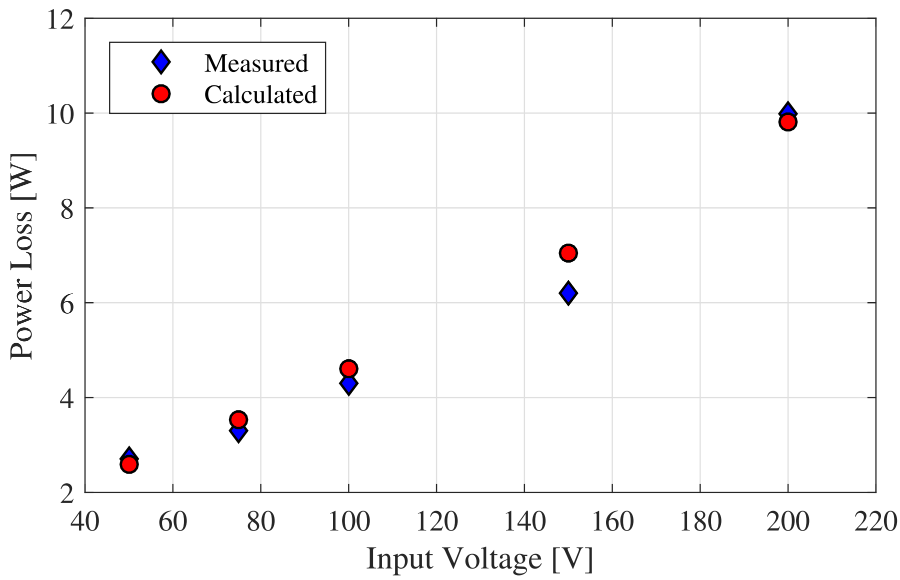

Figure 5.7: Evaluation of model with constant frequency of 100 kHz, duty cycle of 0.7 and output current of 6.67 A.

The error at 150 V is 0.8 W or 12.9 %, which can be seen in Table 5.3. There can be several reasons for this but the one deemed most likely is some error in the measurements. With the justification that the model is accurate at both higher and lower measurement points and in other tests.

Table 5.3: Losses with varying input voltage and constant frequency 100 kHz, duty cycle 0.7 and output current 6.67 A.

Test #	Input Voltage	Meas. Loss	Calc. Loss	Error
3.1	50 V	2.7 W	2.6 W	3.7 %
3.2	75 V	3.3 W	3.5 W	6.1 %
3.3	100 V	4.3 W	4.6 W	7.0 %
3.4	150 V	6.2 W	7.0 W	12.9 %
3.5	200 V	10.0 W	9.8 W	2.0 %

Test 4 - Variation of Input Voltage with $I_{out} = 10$ A

Test 4 was performed in the same way as Test 3 but with increased output current and the result is shown i Figure 5.8 and Table 5.4. Also in this case one point has a larger error than the other measurements.

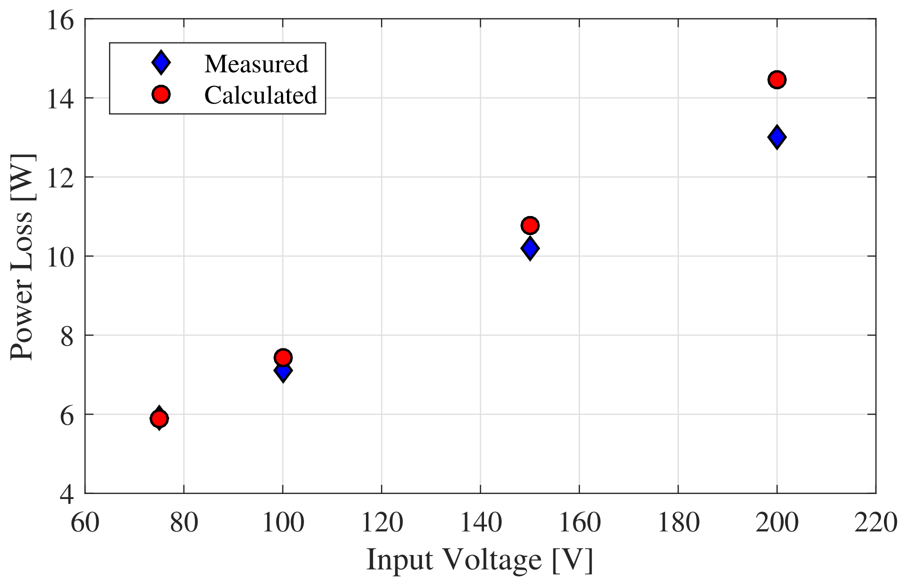

Figure 5.8: Evaluation of model with constant frequency of 100 kHz, duty cycle of 0.7 and output current of 10 A.

In Table 5.4 it can be seen that the error is 1.5 W. The measurements show a tendency of an increased error for increased input voltage. There could be several reasons for this, one being that the accuracy of the model drops with increasing input voltage. This is not deemed the most likely reason or largest contributor to the error due to the good accuracy of the other measurements at 200 V. Another explanation could be a slight different position of the temperature sensor in the AC and DC test, which also would explain the increase in the error due to better cooling at higher temperatures. Regardless, the error equals to 11.5 % which is considered an acceptable error for the model due to other approximations and uncertainties having a larger influence on the loss calculations.

Table 5.4: Losses with varying input voltage and constant frequency 100 kHz, duty cycle 0.7 and output current 10 A.

Test #	Input Voltage	Meas. Loss	Calc. Loss	Error
4.1	75 V	5.9 W	5.9 W	0.0 %
4.2	100 V	7.1 W	7.4 W	4.2 %
4.3	150 V	10.2 W	10.8 W	5.9 %
4.4	200 V	13.0 W	14.5 W	11.5 %

5.3 Winding Loss Evaluation

When evaluating different sources contributing to the winding losses, the model based on the 3.5 kW PQ50/35 test transformer was used for simulations. Both ideal and non-ideal waveforms were used for quantifying different characteristics of the operation of the transformer.

5.3.1 Impact of Waveform and Harmonics

As stated in Section 4.5, the shape of the current waveforms is of great importance when calculating winding losses. The current waveforms are non-sinusoidal and will therefore consist of HF harmonics. This section evaluates the HF characteristics according to (4.17) for two different cases, one with ideal waveforms and one with additional parasitic components introducing HF oscillations and non-idealities, both obtained from circuit simulations using Gecko Circuit. In Figure 5.9 the ideal waveforms are shown, similar to those presented in the theory chapter.

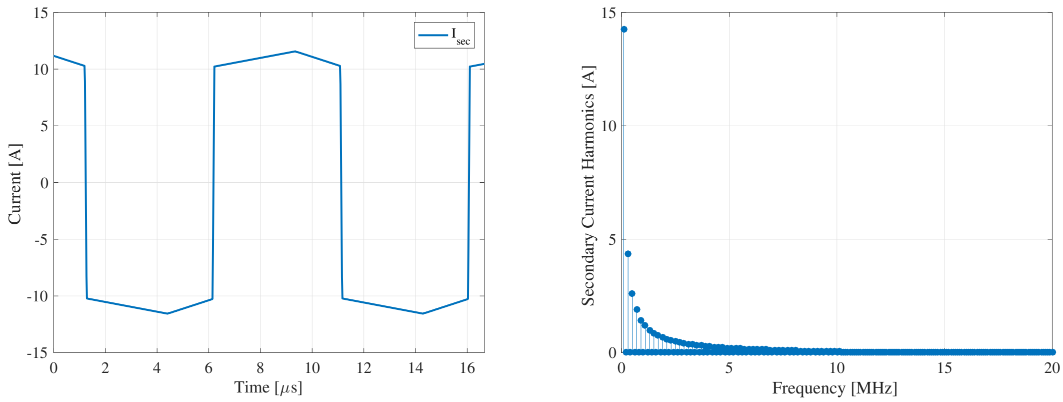

(a) (b)

Figure 5.9: (a) The ideal secondary current operating at 3.3 kW. (b) The frequency spectrum of the secondary current.

In Figure 5.10, HF oscillations are introduced. As discussed earlier, this could for example be caused by the parasitic capacitances of the DC-DC rectifier bridge when oscillating with the leakage inductance of the transformer. As can be seen in 5.10(b), the oscillations causes increased harmonic amplitudes from 9 MHz to 10 MHz.

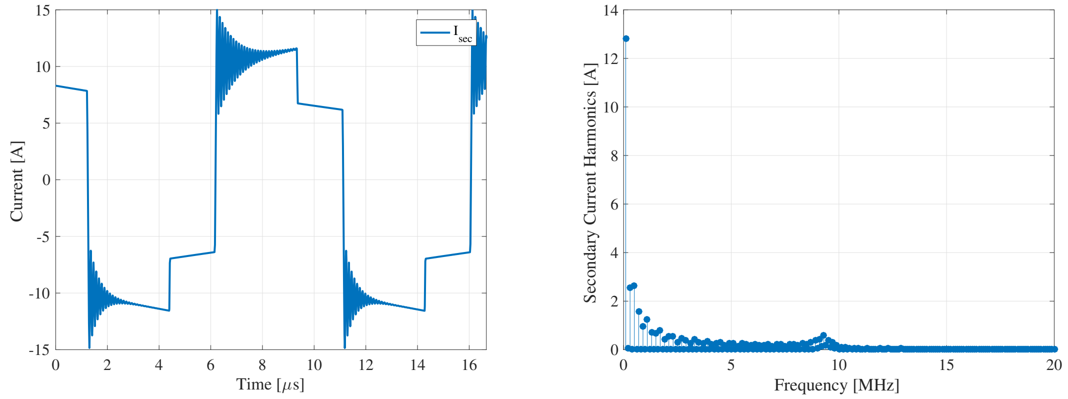

(a) (b)

Figure 5.10: (a) The non-ideal secondary current. (b) The frequency spectrum of the secondary current.

In Figure 5.11(a) the accumulated losses are presented for n number of harmonics. The losses correspond to an operating point at 3.3 kW of power and 11 A of output current. It can be seen that even though the HF resistance is increasing, the amplitude of the current harmonics are not high enough to impact the accumulated loss. It can also be concluded that by only considering the fundamental frequency, the losses will be significantly underestimated.

However, in Figure 5.11(b), the accumulated losses for the non-ideal waveforms are presented for the same operating point but with present oscillations shown in Figure 5.10(a). As can be seen, the increased amplitude of the HF components causes significant loss increase of the oscillations close to 10 MHz.

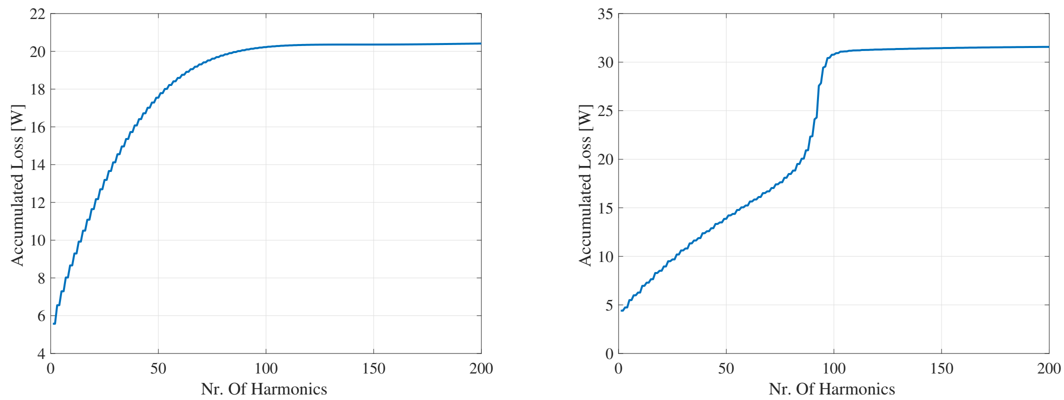

(a) (b)

Figure 5.11: (a) Accumulated losses for ideal current waveforms with n number of harmonics taken into considerations. (b) The accumulated losses when presence of higher amplitudes in the HF harmonics caused by oscillations shown in Figure 5.10.

5.3.2 Interleaving

The theory behind the proximity effect is explained in Section 4.3 and the actual improvements of interleaving are theoretically evaluated in this section. This is done by comparing cases when the number of layers adjacent to each other, M_L, are changed according to (4.14). In these tests, the waveforms are considered ideal and created by simulations for an operating point of 3.3 kW. The results obtained are presented in Table 5.5.

Table 5.5: Winding Losses for different number of layers adjacent to each other $M_L = 1$ and $M_L = 2$.

	Output Voltage	Fundamental	Harmonics	Total
$M_L = 1$	300 V	5.6 W	15.0 W	20.6 W
	350 V	4.1 W	12.1 W	16.2 W
	400 V	3.1 W	10.2 W	13.3 W
$M_L = 2$	300 V	5.8 W	17.7 W	23.5 W
	350 V	4.3 W	14.4 W	18.7 W
	400 V	3.2 W	12.2 W	15.4 W

In this case only four layers are considered for the two different cases ($M_L = 1$ and $M_L = 2$). It can be seen that by simply interleave the layers, losses can be decreased by 12 % to 14 %. According to (4.10), the magnetic field $H_{y,avg}$ depends on both the number of layers N_L and the core winding height h_w. Hence, additional layers and smaller core winding height can be expected to cause higher losses due to the increased magnetic field.

5.3.3 Increased Magnetization Current due to Gap Distance

As mentioned in Section 2.1 the advantages of a larger value of the leakage inductance can be reached by gapping the transformer core. On the other hand, the drawback of this is that it will primarily reduce the magnetization inductance accordingly and therefore increase magnetization current. The magnetization current I_m as a function of gap distance is calculated by FEM simulations and shown in Figure 5.12.

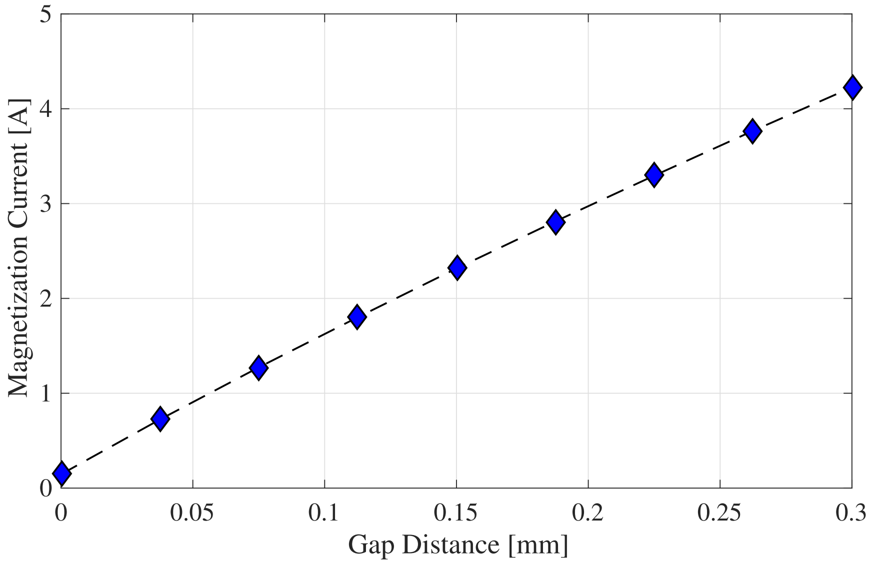

Figure 5.12: The increasing magnetization current amplitude as a function of gap distance for an excitation voltage corresponding to 400 V output voltage at 100 kHz. The current is represented in RMS.

The current I_m is presented by its Root Mean Square (RMS) value and it can be seen that by gapping the transformer with 0.15 mm the magnetization current will increase by a factor of 15 from 0.15 A to 2.17 A compared to the no-gap case. The transformer primary current including I_m will increase accordingly and thereby cause increased losses.

To evaluate the impact of the increased magnetization current, simulations were performed at different values of L_m. The results are presented in Table 5.6.

Table 5.6: Calculated losses as a function of magnetization current.

Air gap	Magnetization Current	Primary Winding Loss
0 mm	0.15 A RMS	1.4 mW
0.11 mm	1.74 A RMS	0.20 W
0.24 mm	3.48 A RMS	0.81 W

As can be seen in Table 5.6 the magnetization current has only a marginal impact on the total winding losses. This can be explained by the low harmonic content of i_m. In Figure 2.2 in Section 2.1 it can be seen that the i_m has a low rate of change, which do not introduce extensive HF harmonics.

5.3.4 Leakage Inductance and its Influence on HF Losses

The value of the leakage inductance L_σ is not only important for achieving ZVS. It is also important because it affects the steepness of the current change in a transition from passive to active state, hence the content of harmonics. By simulations this have been evaluated and the results are shown in Figure 5.13.

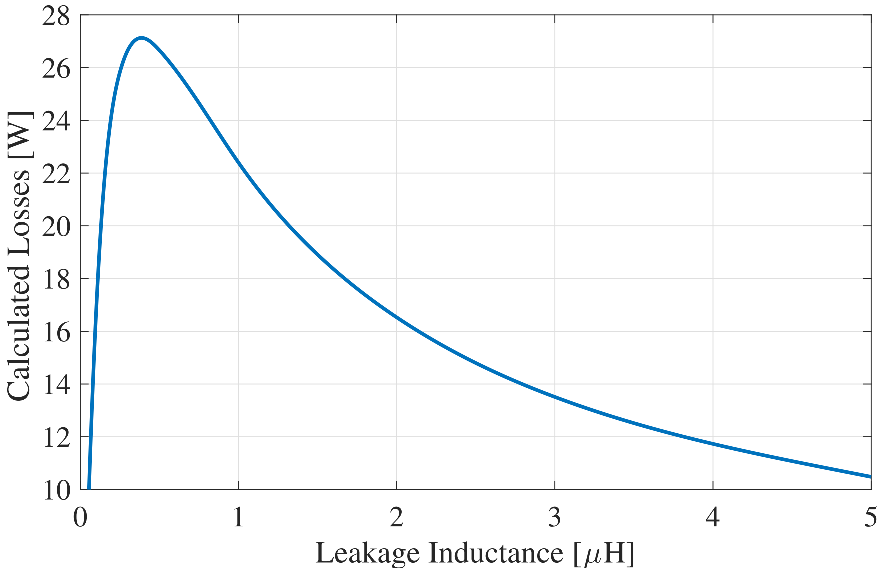

Figure 5.13: Total winding losses at 3.3 kW of output power and L_m is 163 µH.

As can be seen in Figure 5.13 the leakage inductance have a significant impact on the losses. A very small leakage inductance leads to relatively low losses, which is desired. However, this is nothing to strive for since in this operation the energy in the leakage inductance will be fully drained during a transition and therefore ZVS will be lost according to (2.2). Moreover, it can be seen that for high values of L_σ, the losses decreases. This can be explained by the reduced current steepness, as previously mentioned. For high di/dt the harmonics will be distributed with higher amplitudes at higher frequencies thus leading to more losses due to the increased HF resistance.

5.3.5 Impact of Strand Diameter

The current waveforms can as seen in previous sections change significantly depending on the properties of the transformer and the converter. For example, the oscillations introduced by the resonance between the leakage inductance and the parasitic capacitance of the rectifier diodes. These oscillations can in turn be effectively eliminated by proper implementation of snubber circuits. Furthermore, both the input voltage and the leakage inductance have an impact on the di/dt of the current transitions, which highly affect the harmonic content of the waveforms.

Because of the reasons mentioned above was the optimal strand diameter optimized with respect to power loss rather than AC resistance as in Section 4.6. In this way, the resistance is weighted against the amplitudes of the current harmonics and the lowest overall losses can be achieved.

To evaluate the impact of strand diameter and to find the optimal, first the parameters for (4.18) have to be found. This was done by performing a LMS optimization on wire data provided by manufacturers. All further optimizations regarding optimal strand diameter was performed considering litz wires from Elektrisola with double serving and grade 1. The parameters for this wire equals to $\alpha = 1.223$ and $\beta = 0.965$, with a reference diameter $d_r = 0.079\,\text{mm}$ [21].

In Figure 5.14 the optimal strand diameter is evaluated for ideal waveforms with frequency of 100 kHz and the outer diameter of the conductor is set to 2 mm. The operating point is an output voltage of 275 V and an output power of 3.5 kW.

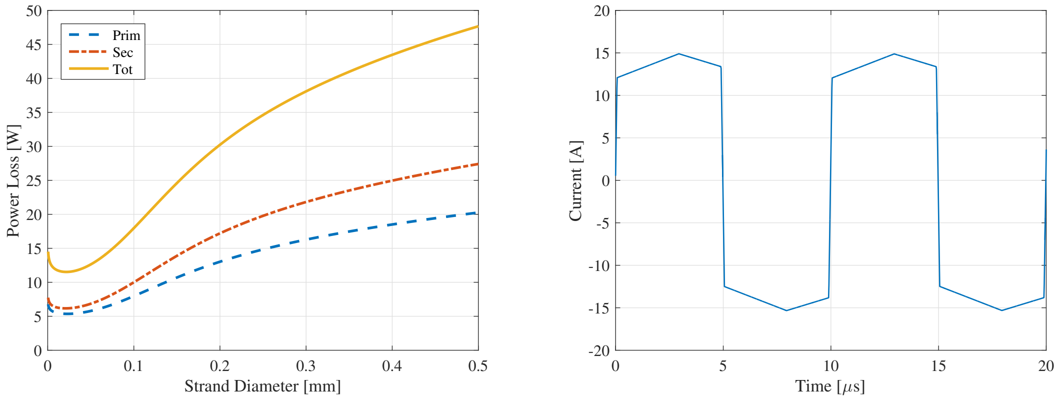

(a) (b)

Figure 5.14: (a) Impact of strand diameter on winding losses for ideal current waveforms seen in (b) with 200 harmonics taken into considerations. (b) Secondary current on test transformer with an output voltage of 275 V and output power of 3.5 kW.

In Figure 5.15 the same operating point is considered, but in this case, with added non-idealities. This results in a resonance tank that introduces HF oscillations, thus affecting the optimal strand diameter.

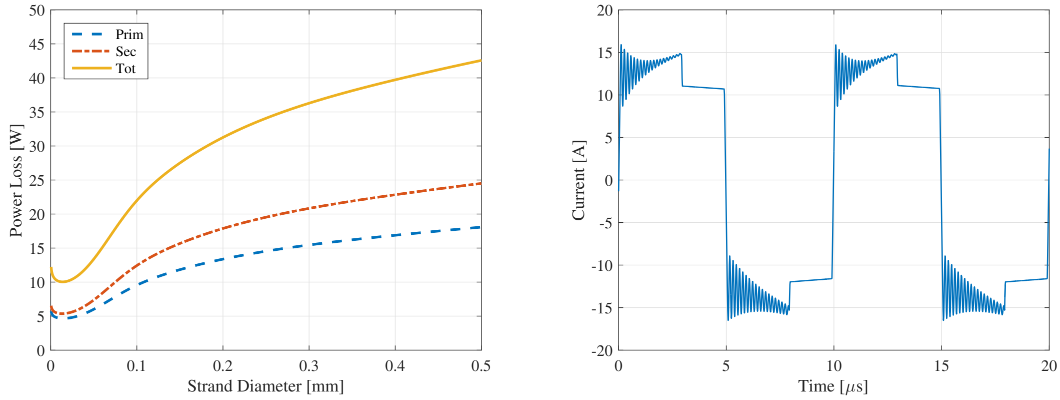

(a) (b)

Figure 5.15: (a) Impact of strand diameter on winding losses for non-ideal current waveforms seen in (b) with 200 harmonics taken into considerations. (b) Secondary current with an output voltage of 275 V and output power of 3.5 kW.

The power loss contribution of the fundamental component and the harmonics is highly dependent on the winding configuration, as seen in Figure 5.14 and Figure 5.15. To evaluate this further the losses were separated into fundamental component and harmonics and calculated for four different litz wires. The result of the calculations are presented in Table 5.7. It can be seen that the oscillations have a significant impact on the losses and should therefore be minimized by proper implementation of snubbers. It can further be seen that non-ideal waveform has a lower fundamental loss component which is due to the drop in current seen in Figure 5.15(b).

Table 5.7: Winding loss contribution of fundamental component and harmonics for four different litz-wires with an outer diameter of 2 mm. Output power 3.5 kW and output voltage 275 V.

	Impact of strand diameter and waveform			
	Wire	Fundamental	Harmonics	Total
Ideal	630 x 0.05 mm	9.1 W	3.5 W	12.6 W
	250 x 0.08 mm	9.1 W	6.4 W	15.5 W
	165 x 0.1 mm	9.3 W	8.7 W	18.0 W
	85 x 0.14 mm	9.8 W	13.5 W	23.3 W
Non-Ideal	630 x 0.05 mm	7.8 W	5.6 W	13.4 W
	250 x 0.08 mm	7.8 W	11.0 W	18.8 W
	165 x 0.1 mm	7.9 W	14.1 W	22.0 W
	85 x 0.14 mm	8.3 W	18.3 W	26.6 W

As can be seen in Table 5.7, the total losses are increased with the introduction of non-idealities. However, the difference is not excessively large which can be explained by the decreased loss contribution from the fundamental component. In

Figure 5.15(b) the current drop that lowers the amplitude of the fundamental component, thus lowering the fundamental amplitude.

It can furthermore be seen that, for the non-ideal case, the optimal strand diameter is 0.025 mm. However, the selection of litz wires are not only determined by loss reductions, but also the commercial availability of wire dimensions. Litz wires with small cross sections are difficult to manufacture and will increase in price with decreasing strand diameter. Because of this, as in many other cases, it is desired to select litz wire based on a weighting between cost and performance.

5.4 Core Loss Evaluation

Primarily, the core loss is desired to be calculated by Steinmetz equations, found in Section 3.2. However, by FEM simulations, the magnetic flux density can be evaluated in 3D, which allows for more accurate loss calculations by considering inhomogeneous flux distribution. In FEM simulations, the magnetic flux density amplitude should not be considered as the exact truth but instead as a hint of where the magnetic flux reaches its maximum. This due to the crucial requirements of correct material parameters. An example of this simulation is presented in Figure 5.16(a).

5.4.1 Inhomogeneous Flux Distribution

In Figure 5.16, a FEM simulation of the transformer core is presented. It can be seen that the flux density is not equally distributed within the core and this might result in inaccurate approximations with the formulas presented in Section 3.2, where the flux density is assumed to be constant. It can also be seen that the highest flux densities are present around sharp edges, as expected.

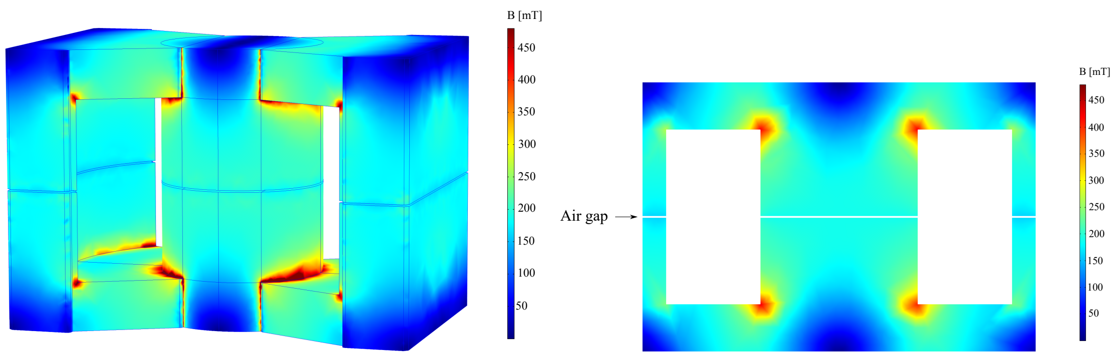

(a) (b)

Figure 5.16: (a) Magnetic flux density distribution within the core at an excitation corresponding to 400 V output voltage. (b) The peak flux density $\hat{B}$ within the core for an excitation voltage corresponding to 400 V output voltage at 100 kHz. The air gap is 0.22 mm.

5.4.2 Comparison of FEM Results and Steinmetz Equations

Normally, E-cores are considered having a homogeneous flux distribution, hence Steinmetz equations can be applied. When using a different core types, it is interesting to evaluate the impact from inhomogeneous flux distribution. Results from FEM simulations can be compared with the analytical OSE results since both methods are based on the same equation and data. By this, a conclusion of the influence of inhomogeneous flux distribution on the calculations can be made. The comparison is shown in Figure 5.17. Additionally, results from iGSE, which in contrast also is considering the rate of change in flux, are shown in the same figure.

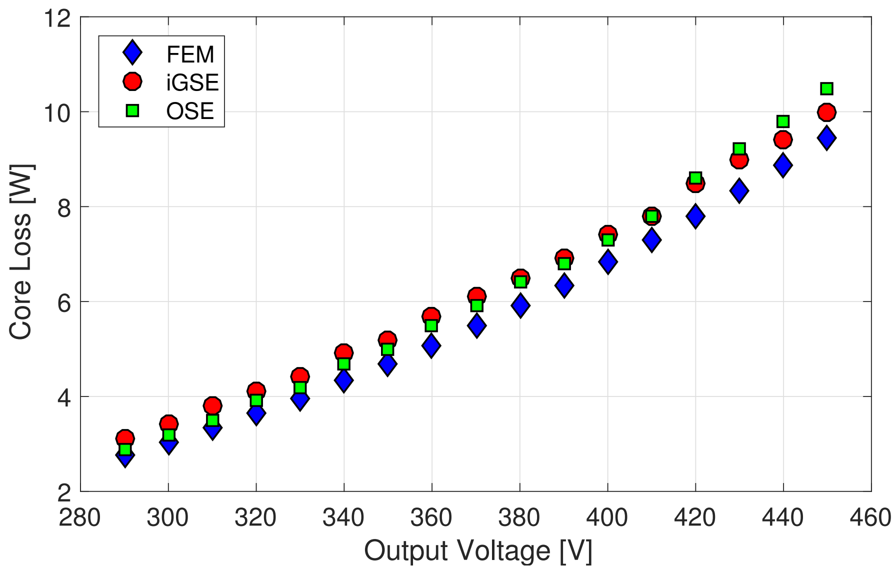

Figure 5.17: Comparison of results from analytical OSE and iGSE equations together with results from FEM simulations based on OSE with $N_p = 14$ turns, 0.22 mm air gap and a switching frequency of 100 kHz.

It can be seen that with increasing output voltage (i.e. increased magnetization), the deviations between FEM and OSE results are increasing. It should also be pointed out that the iGSE and FEM results are similar throughout the full range disregarding an offset in the order of 0.6 W. The OSE results, which are expected to be the most inaccurate, increases the deviation from FEM simulations at higher voltages. This might be due to that the GSE formula does not account for the rate of change in flux, in contrast to iGSE.

6 Transformer Design Proposal for an Isolated 11 kW DC-DC Stage

For the design of the isolated DC-DC stage in the 11 kW OBC, modular blocks of 5.5 kW are proposed to achieve the desired power rating. In Figure 6.1 the proposed topology of two parallel full bridge converters is shown. The block can further be used in OBCs of higher power ratings by paralleling of more blocks, with minimal design effort. Hence, the power rating of the designed transformer is 5.5 kW.

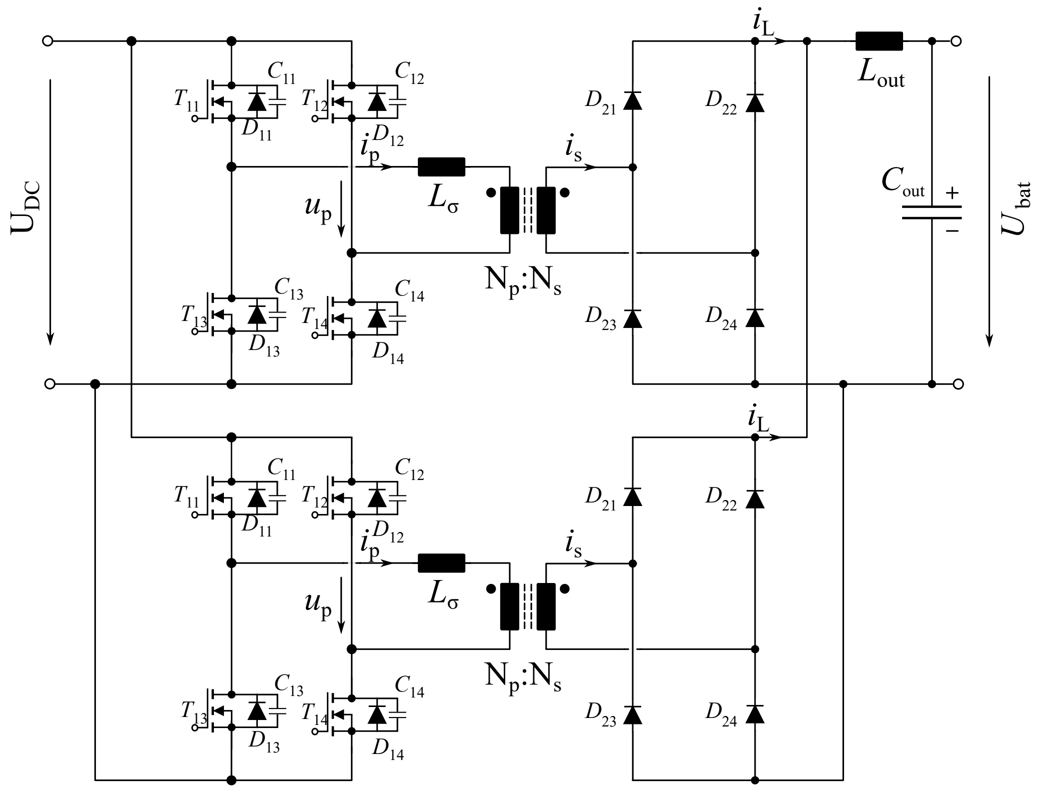

Figure 6.1: Topology of proposed realisation of the isolated DC-DC stage for the 11 kW OBC, with two parallel full bridge isolated DC-DC converters.

6.1 Multi-Object Optimization

The design procedure of the 5.5 kW transformer is based on the developed transformer model extended to a multi-object optimization, a so called Pareto optimization. The optimization was performed with respect to power density and efficiency.

6.1.1 Design Algorithm

The design is initialized by the definition of the system specifications, including input voltage U_{in}, output voltage U_{out}, output power P_{out}, minimum allowed turns ratio n_{min}, etc. All input parameters for the system specification can be seen in Figure 6.2, where the entire design algorithm is presented. Furthermore, the properties of a number of commercially available cores are loaded into the design routine.

In the second step of the algorithm all possible turns ratios are calculated based on two conditions: peak flux density in the core $\hat{B}_{min} \leq \hat{B} \leq \hat{B}_{max}$ (determines primary turns) and minimum turns ratio $n \geq n_{min}$ (determines secondary turns). An individual winding configuration is then created for each combination of cores and turns ratios n. The winding configuration is aimed to maximize the fill factor of the core window and is performed for two different cases γ.

In the first case $\gamma = 1$, the primary and secondary winding consists of one wire each. In the second case $\gamma = 2$, both windings are made up of two parallel wires instead of one, which is better suited for high and narrow core windows. A litz wire is then created with the resulting conductor diameter d_{litz} and a defined strand diameter d_{cu}. Finally, all winding configurations that result in an optimal number of layers $M_N = 3$ (primary + secondary layers) are disregarded. This is because of the lack of viable solutions with full layers of primary and secondary windings for the particular turns ratio n.

In the next step, ideal waveforms as in Figure 2.2 are created in Matlab from system specifications. This is done for all different combinations of turns ratios n. Lastly, the winding and core losses are calculated in the same manner as in Section 5.1.

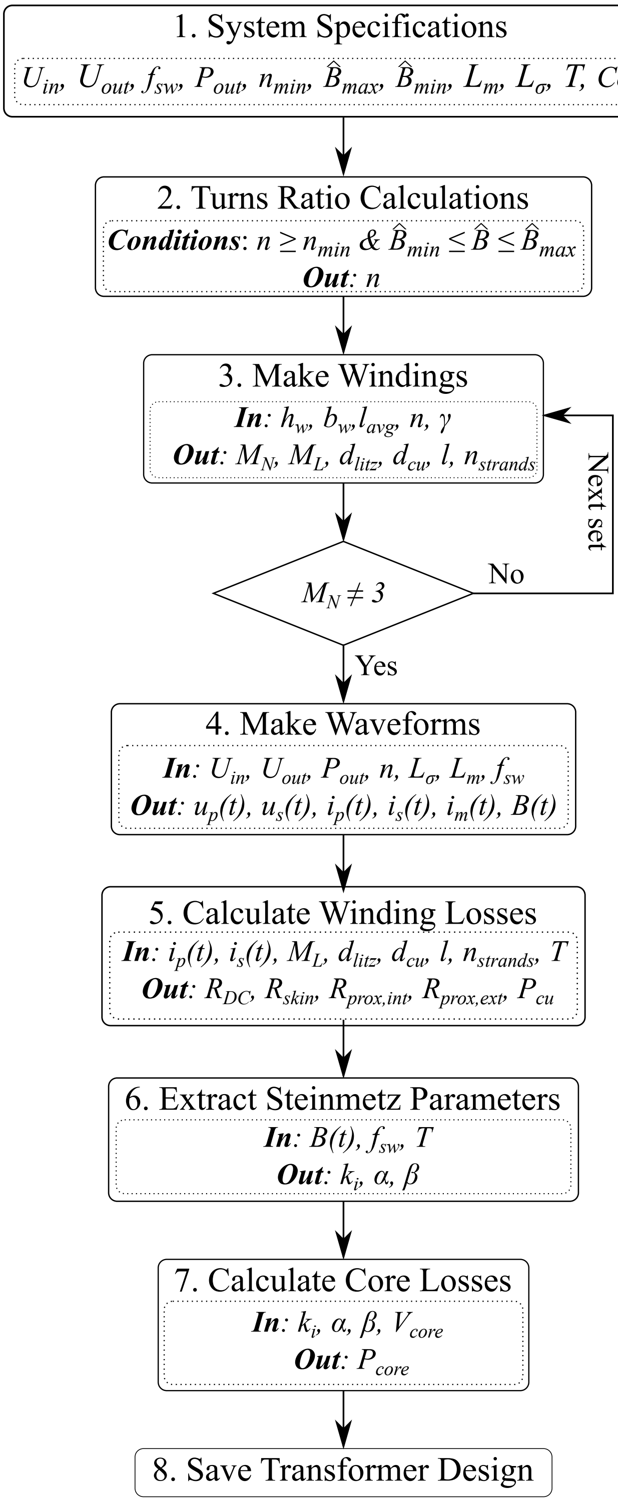

Figure 6.2: Algorithm for the Pareto optimization of the transformer design. In each step the ingoing parameters or conditions are displayed together with the output parameters of each step.

6.1.2 Pareto Optimization

The Pareto optimization was performed with system specifications as in Table 6.1. When operating in the lower range of output voltage, the output current of one transformer increase to 20 A, resulting in high winding losses. In contrast, at high output voltages, the output current decreases and the core magnetization increase, resulting in higher core losses. Consequently, it is desirable to design a transformer with optimal distribution between winding losses and core losses throughout the full operating range.

Table 6.1: System specifications for the Pareto optimization.

Parameter	**Value**
Output power, P_{out}	5.5 kW
Input voltage, U_{in}	650 V to 750 V
Output voltage, U_{out}	275 V to 470 V
Frequency, f_{sw}	100 kHz to 180 kHz
Leakage inductance, L_σ	2.5 µH
Magnetization inductance, L_m	300 µH
Peak flux density, $\hat{B}$	150 mT to 250 mT
Minimum turns ratio, n_{min}	$750/470 \cdot 0.9$
Temperature, T	100 °C

The optimization is performed as a weighting of the two critical points. The first being at maximum output voltage, resulting in the maximum core magnetization and consequently the highest core loss. The other point is at minimum output voltage, resulting in maximum output current, giving the maximum winding losses. The weighting is done with a contribution of 50 % from each. Furthermore, all other operating points will have losses in the range between these two critical points and no Pareto optimization have to be made for these points.

The result of the Pareto optimization is shown in Figure 6.3. Each dot represents a possible transformer design, with the color being determined by the switching frequency. Each vertical line of designs represent a specific core, since the volume is independent of the winding configuration. Figure 6.3 furthermore shows the selected transformer design, which was chosen due to an even distribution between losses in the core and the winding. It further has an even distribution between the total losses in the two critical cases.

In the designs that have a higher power density than the chosen one, the winding loss contribution is increased both with respect to core losses and winding losses in larger designs. This results in higher heat dissipation from the windings and aggravates the cooling of the transformer in addition to the already higher heat dissipation per area unit, which is not desirable. For these reasons, a design with higher power density than the chosen is not considered. Furthermore, designs of the same core with higher weighted efficiency are not chosen due to a worse distribution between core and winding losses. A slightly lower power density could have been chosen with a small increase of the efficiency, but the increase in power density was chosen over the efficiency.

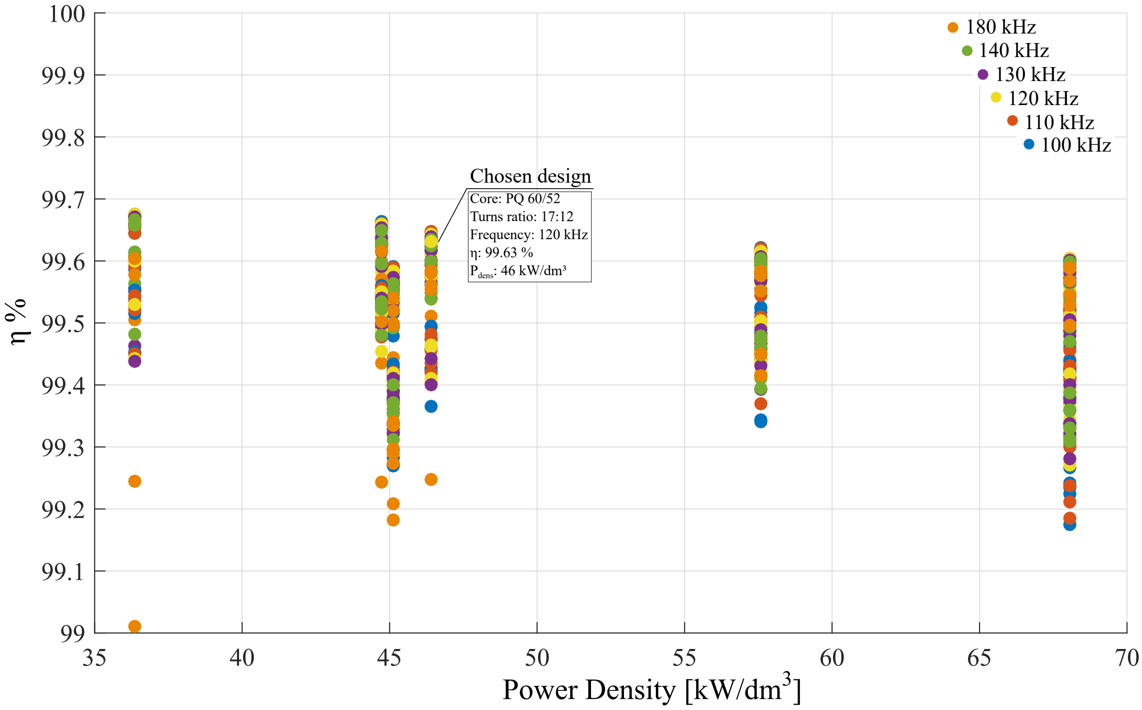

Figure 6.3: Optimization of the transformer design as a function of power density and efficiency. Each point represent a transformer design and the efficiency is an weighting between max current and max voltage operation.

6.2 Core and Winding Selection

The properties of the selected design with its specifications is presented in Table 6.2. To be able to fully utilize the core window but still avoid using an excessive number of strands the design key is to connect two windings in parallel. This is done both on the primary winding and on the secondary winding. Although, the turns ratio is kept to 17/12. By this, the cost of the windings is reduced at the same time as winding losses are reduced.

Table 6.2: Specifications of proposed 5.5 kW transformer.

Core:	PQ 60/52
Core material:	PC47
Primary winding:	2 x (317 x 0.08 mm)
Secondary winding:	2 x (427 x 0.08 mm)
Turns ratio:	17:12
Frequency:	120 kHz
Power rating:	5.5 kW
Efficiency η:	99.63 %

As can be seen in Table 6.2, an efficiency of 99.63 % can be expected, assuming ideal waveforms (without externally caused oscillations).

Moreover, Figure 6.4 visualizes the winding layer configuration. The windings are interleaved and consists of three primary and two secondary layers. As previously mentioned, one conductor is connected in parallel with its vertical neighbor as seen in Figure 6.4. This has two main advantages, the first being the different winding geometry which is beneficial for high and narrow core windows. The other one being the use of smaller wire diameters, which are more commercially available, without significantly reducing the copper fill factor.

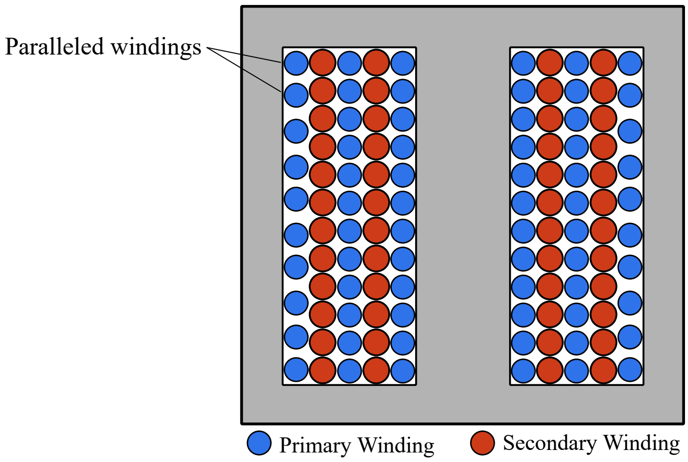

Figure 6.4: Winding configuration of proposed transformer design.

In Figure 6.5 the selected PQ60/52 core with dimensions 60 x 39 x 52 mm is visualized. The volume is 115 % bigger than the core used for the 3.5 kW transformer, but with increased efficiency. The maximum peak flux density $\hat{B}$ for the core in the operating range equals to 176 mT at 470 V output voltage

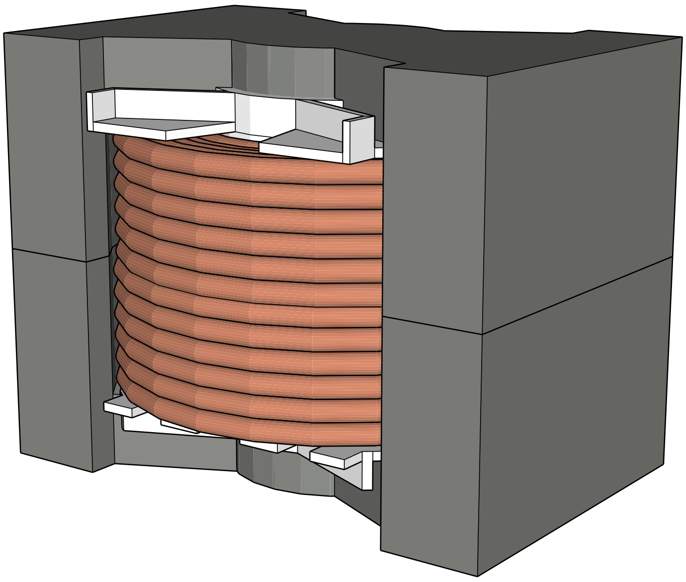

Figure 6.5: CAD drawing of the proposed design with a PQ 60/52 core.

6.3 Loss Evaluation for Selected Core

The selected transformer is evaluated at different operating points for determining its full range performance. Ideal waveforms are used for this case with an output power P_{out} of 5.5 kW. At low output voltages, the input voltage is kept constant at 650 V whilst on higher output voltages, the duty cycle D is limited to 0.9. Hence, the input voltage is increased. As can be seen in Table 6.3 the transformer is expected to have best performance for output voltages between 365 V and 395 V with an efficiency of 99.68 %.

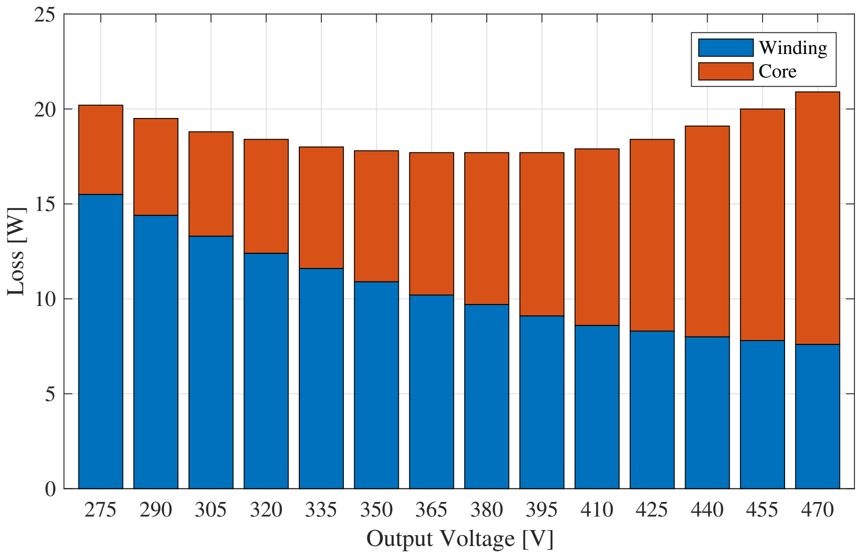

Figure 6.6: Operating points with separated losses at 5.5 kW output power. $L_\sigma = 2.5\,\mu\text{H}$ and $L_m = 300\,\mu\text{H}$.

The calculated losses are furthermore graphically presented in Figure 6.6 where it can be seen that for low output voltages, the winding losses are dominant due to the high current. The winding losses are reduced with increased output voltage whilst the core losses are increased due to higher magnetization. This is an expected behaviour and the design is deemed to be well balanced by means of winding and core losses through out the full operating range.

Table 6.3: The winding and core losses for 14 operating points.

Input Voltage	**Output Voltage**	**Output Current**	**Core Losses**	**Winding Losses**	**Total Losses**
650 V	275 V	20.0 A	4.7 W	15.5 W	**20.2 W**
650 V	290 V	19.0 A	5.1 W	14.4 W	**19.5 W**
650 V	305 V	18.0 A	5.5 W	13.3 W	**18.8 W**
650 V	320 V	17.2 A	6.0 W	12.4 W	**18.4 W**
650 V	335 V	16.4 A	6.4 W	11.6 W	**18.0 W**
650 V	350 V	15.7 A	6.9 W	10.9 W	**17.8 W**
650 V	365 V	15.1 A	7.5 W	10.2 W	**17.7 W**
650 V	380 V	14.5 A	8.0 W	9.7 W	**17.7 W**
650 V	395 V	13.9 A	8.6 W	9.1 W	**17.7 W**
650 V	410 V	13.4 A	9.3 W	8.6 W	**17.9 W**
669 V	425 V	13.0 A	10.1 W	8.3 W	**18.4 W**
693 V	440 V	12.5 A	11.1 W	8.0 W	**19.1 W**
716 V	455 V	12.1 A	12.2 W	7.8 W	**19.9 W**
749 V	470 V	11.8 A	13.3 W	7.6 W	**20.8 W**

7 Conclusions

7.1 Results from Present Work

In this work, the main sources of winding losses in HF transformer are explained physically and quantified by simulations and measurements. It is possible to conclude that a thorough design could significantly reduce losses and the number of expensive purchase-and-test-iterations. The major contribution to the winding losses, often neglected, is the current harmonics present in a non-sinusoidal waveform. It is shown that only considering the fundamental frequency in loss calculations could result in a significant underestimation of the actual losses.

As in many other cases, individual electrical components will not act ideally due to the influence from other components. In this thesis, this is evaluated by measurements and analyzes by calculations. The findings of this is that parasitic capacitances of a potential diode rectifier may introduce HF oscillations which significantly affect the accumulated losses in the windings.

Finally, the proposed 5.5 kW transformer for use in a 11 kW DC-DC stage is a design that has a even distribution of losses within the operating range and reaches an efficiency of 99.63 % or above in the entire range.

7.2 Future Work

When developing models of a real system the accuracy and coherence between the two are of significant importance. By performing steady-state temperature measurements it is possible to get a good approximation of the present losses. However, it should be mentioned that a trustful model should be carefully evaluated throughout its full operating range. In this work, due to limitations of the measurement setup, the operating points evaluated were limited to 1340 W and 250 V. Additionally, the accuracy of the measurements could be further improved by using several sensors as well as a fixed measurement module to ensure that measurement errors are reduced.

As presented in the report, the magnetization inductance L_m and its current is of minor importance for the winding losses within a reasonable range. However, it is also shown that the value of the leakage inductance L_σ affects the harmonic distribution thus also the losses. In this thesis the leakage inductance are for the 3.5 kW transformer case measured, but for the 5.5 kW design case it is approximated. For future work, an implementation of a leakage inductance calculation would be desirable. This could for example be done by integrating more advanced FEM calculations.

Furthermore, the dependency of semiconductors non-idealities should be evaluated further. As seen in this work, the selected semiconductors can have a significant impact on the performance of the transformer and the complete system. The transformer should therefore be integrated in a real isolated DC-DC stage with real semiconductors to fully evaluate the dependency of their electrical properties and non-idealities.

Lastly, the main reason besides efficiency of why it is desirable to reduce losses, is the thermal perspective. The unit should not overheat during operation and the lifespan of the components is prolonged with reduced temperatures. In this work the thermal properties have not been within the main scope of the investigation. Instead the focus have been on quantifying and minimizing the losses and consequently, the heat dissipation. A natural continuation of this work would therefore be to include thermal modeling in the design procedure of the transformer.

As mentioned in the introduction, cooling of OBCs is fundamentally different then cooling of most other equipment due to the lack of fans and forced convection. The system is instead water cooled with the existing cooling system of the vehicle. Therefore, how to distribute the winding and core losses is also a question of where it is possible to perform cooling. By implementing multi-physical simulations, thermal properties and electrical properties could be joined for evaluating the system overall performance in typical OBC applications.

Bibliography

[1] F. Bedell, "History of A-C Wave Form, Its Determination and Standardization," *American Institute of Electrical Engineers*, vol. 61, no. 12, pp. 864–868, 1942.

[2] W. G. Hurley and W. H. Wölfle, *Transformers and Inductors for Power Electronics : Theory, Design and Applications*. Wiley, 2013.

[3] J. Muhlethaler, J. Biela, J. W. Kolar, and A. Ecklebe, "Improved Core-Loss Calculation for Magnetic Components Employed in Power Electronic Systems," *IEEE Transactions on Power Electronics*, vol. 27, pp. 964–973, Feb 2012.

[4] J. Li, T. Abdallah and C. Sullivan, "Improved calculation of core loss with nonsinusoidal waveforms," in *Industry Applications Conference, 2001*, vol. 4, pp. 2203–2210, Sept 2001.

[5] K. Venkatachalam, C. Sullivan, T. Abdallah and H. Tacca, "Accurate prediction of ferrite core loss with nonsinusoidal waveforms using only steinmetz parameters," in *Computers in Power Electronics, 2002. Proceedings.*, pp. 36–41, June 2002.

[6] J. Muehletaler, *Modeling And Multi-Objective Optimization Of Inductive Power Components*. PhD thesis, ETH Zurich, 2012.

[7] C. R. Sullivan, "Optimal choice for number of strands in a litz-wire transformer winding," *IEEE Transactions on Power Electronics*, vol. 14, pp. 283–291, Mar 1999.

[8] H. J. Chae, W. Y. Kim, S. Y. Yun, Y. S. Jeong, J. Y. Lee, and H. T. Moon, "3.3 kw on board charger for electric vehicle," in *Power Electronics and ECCE Asia (ICPE ECCE), 2011 IEEE 8th International Conference on*, pp. 2717–2719, May 2011.

[9] J. S. Lai, H. Miwa, W. H. Lai, N. H. Tseng, C. S. Lee, C. H. Lin, and Y. W. Shih, "A high-efficiency on-board charger utilitzing a hybrid llc and phase-shift dc-dc converter," in *Intelligent Green Building and Smart Grid (IGBSG), 2014 International Conference on*, pp. 1–8, April 2014.

[10] B. R. Lin and T. Y. Shiau, "Zero-voltage switching full-bridge DC/DC converter with parallel-connected output and without output inductor," *IET Power Electronics*, vol. 6, pp. 505–515, March 2013.

[11] M. Rylko, K. Hartnett, J. Hayes and M. Egan, “Magnetic material selection for high power high frequency inductors in dc-dc converters,” in *Applied Power Electronics Conference and Exposition, 2009*, pp. 2043–2049, Feb 2009.

[12] [Online] Ferroxcube, “3C95 Datasheet.” `http://www.ferroxcube.com/`, 2016. [Accessed 4-Apr-2016].

[13] M. A. Bahmani, E. Agheb, T. Thiringer, H. K. Hidalen and Y. Serdyuk, “Core loss behavior in high frequency high power transformers - i: Effect of core topology,” *Journal of Renewable and Sustainable Energy*, vol. 4, no. 3, 2012.

[14] R. W. Erickson and D. Maksimović, *Fundamentals of Power Electronics*. University of Colorado, 2 ed., 2001.

[15] C. P. Steinmetz, “On the law of hysteresis,” *American Institute of Electrical Engineers Transactions*, vol. 9, pp. 3–64, 1892.

[16] J. Reinert, A. Brockmeyer and R. W. De Doncker, “Calculation of losses in ferro- and ferrimagnetic materials based on the modified steinmetz equation,” *Industry Applications Conference*, vol. 3, pp. 2087–2092, 1999.

[17] J. Pedro, “Electromagnetic modeling by finite element methods,” *Markel Dekker*, 2003.

[18] N. Mohan, T. M. Undeland, and W. P. Robbins, *Power Electronics, Converters, Applications and Design*. John Wiley & Sons Inc, 3 ed., 2003.

[19] J. Biela, *Optimierung des elektromagnetisch integrierten Serien-Parallel-Resonanzkonverters mit eingeprägtem Ausgangsstrom*. PhD thesis, ETH Zurich, 2005.

[20] V. Valchev and A. Van den Bossche, *Inductors and Transformers for Power Electronics*. CRC Press, 2005.

[21] Elektrisola, “Technical Data (metric) acc. to NEMA MW1000C.” `https://www.elektrisola.com/enamelled-wire/technical-data-by-size/nema-mw1000c-metric.html`. Online; accessed 13 April 2016.